FULL PAPER Open Access



Temporal variation in the cloud-top temperature of Venus revealed by meteorological satellites

Gaku Nishiyama^{1,2,3}, Yudai Suzuki⁴, Shinsuke Uno^{5,12}, Shohei Aoki⁶, Tatsuro Iwanaka⁶, Takeshi Imamura⁶, Yuka Fujii³, Thomas G. Müller⁷, Makoto Taguchi⁸, Toru Kouyama⁹, Océane Barraud¹, Mario D'Amore¹, Jörn Helbert^{1,10}, Solmaz Adeli¹ and Harald Hiesinger¹¹

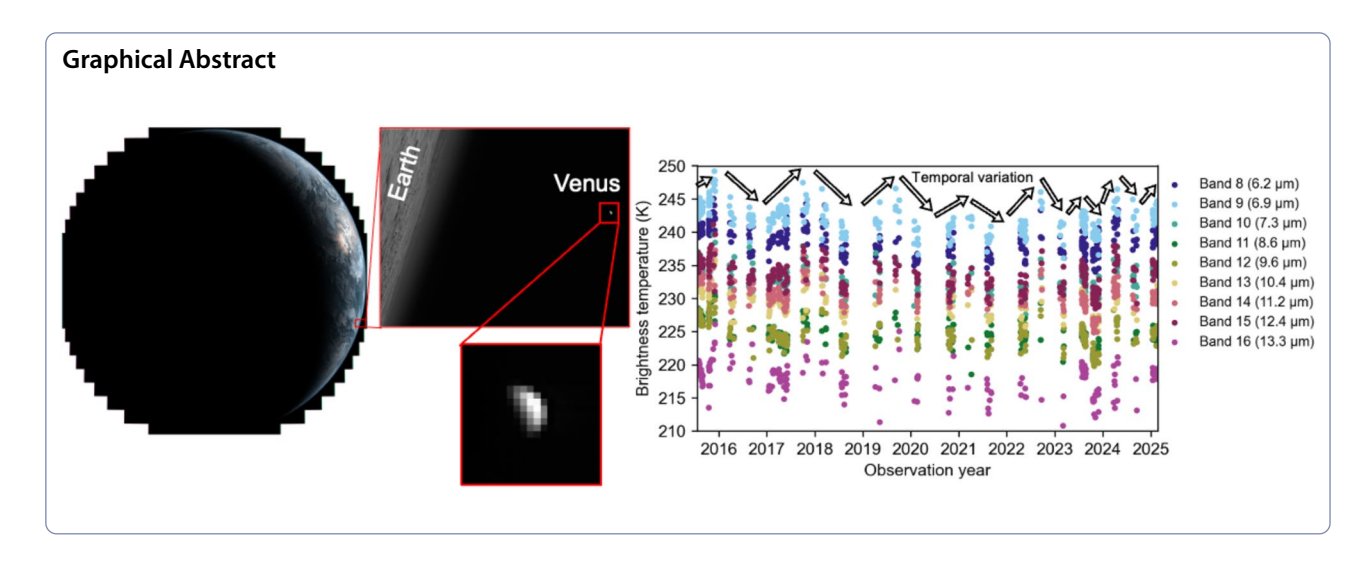
Abstract

Temporal variations in the cloud-top temperature of Venus are essential observable for understanding its atmospheric dynamics and related phenomena, such as thermal tides and planetary-scale waves. While multiband monitoring of both phenomena over years could hint at ongoing dynamics, spaceborne observations of Venus over the last decade are limited to single-band imagery or short timeframe. As a complementary data for the lack of decadal multiband infrared measurements of Venus, the Japanese meteorological satellites Himawari-8/9 may be utilized because they have been coincidentally imaging Venus in space adjacent to the Earth's rim. These images can serve as a new dataset for both Venus science and instrument calibrations in planetary missions, though they have never been utilized for such purposes. This study first archived all the Venus images taken by Himawari-8/9 from July 2015 to February 2025 and succeeded in retrieving disk-normalized brightness temperatures and their temporal variation on day to year scales. The archived data were compared with other observations from the Akatsuki and BepiColombo missions. Our comparison shows that the long-wave infrared camera (LIR) on Akatsuki has underestimated the infrared radiance by 15–17%, which needs to be considered in future LIR data analyses. From comparisons of the observed temperatures at each local time on Venus, we also found that the retrieved temporal variations contain changes in the patterns of thermal tides. Particularly at sunrise, the observed brightness temperatures were not constant between 2015 and 2024, implying variations in the amplitude of diurnal thermal tides. Furthermore, the amplitude of the 5-day Rossby waves decreased at altitudes of 68 km or higher, as suggested by previous numerical circulation models. Although retrieval of the Rossby-wave amplitude was successful only in two observation periods, a variation in altitude dependence was confirmed between 2015 and 2024. These observed temporal variations may be caused by several factors, including a change in static stability observed in the Himawari-8/9 measurements. These results demonstrate that meteorological satellites can serve as additional eyes to access the Venusian atmosphere from space and complement future observations from planetary missions and ground-based telescopes.

Keywords Venus, Infrared spectrum, Temperature, Atmosphere, Himawari-8/9, Akatsuki, BepiColombo, Thermal tide, Rossby wave

*Correspondence: Gaku Nishiyama gaku.nishiyama@dlr.de Full list of author information is available at the end of the article





1 Introduction

Venus is an important target among our solar system bodies to monitor constantly at mid-infrared wavelengths because of the temporal variability of its thermal structure. The cloud-top temperature of Venus exhibits several distinctive structures associated with its atmospheric dynamics. For instance, the temperature field displays a solar-fixed pattern known as thermal tides, which are global-scale waves excited by solar heating. The thermal tides are thought to play a key role in driving the superrotation of the Venus atmosphere because their vertical propagation contributes to the transport of angular momentum (e.g., Fels and Lindzen 1974; Plumb 1975; Hou et al. 1990; Newman and Leovy 1992; Takagi and Matsuda 2007). Numerical studies show that the structure of thermal tides is highly sensitive to factors such as zonal wind speed and static stability (e.g., Takagi and Matsuda 2005; Suzuki et al. 2022). Therefore, monitoring the temporal evolution of thermal tides is essential for understanding the variations within the Venusian atmosphere. Furthermore, the Venus atmosphere is known to host planetary-scale Kelvin and Rossby waves, whose circulation periods are around 4 days for Kelvin and 5-6 days for Rossby waves (Rossow et al. 1990; Imai et al. 2019; Nara et al. 2019; Kajiwara et al. 2021; Lai and Li 2023). These waves have been the target of previous Venus observations as they are also expected to contribute to momentum transport (Del Genio and Rossow 1990; Yamamoto and Tanaka 1997; Imamura et al. 2004; Imamura 2006). The vertical structure of these planetary-scale waves may also be influenced by factors like the zonal wind speed (Kouyama et al. 2015). Retrieval of altitudinal information and its temporal variation is crucial for a comprehensive understanding of Venusian atmospheric dynamics.

Despite the importance, the temporal coverage of Venus's temperature measurements remains limited to specific timeframes. While multiple space exploration missions have conducted Venus observations, no orbiter has continuously monitored Venus for more than a decade. Spaceborne mid-infrared observations have been restricted to the durations of several space missions: the Venera-15 and 16 missions in 1983 (e.g., Oertel et al. 1985), the Pioneer Venus Orbiter from 1978 to 1979 (e.g., Taylor et al. 1980), and the Planet-C/Akatsuki mission from 2015 (e.g., Nakamura et al. 2016). Only the Akatsuki mission has been able to achieve a sufficient long-term observation of the Venus temperature for a decade, although the communication to the spacecraft is not established at present due to its attitude issue. Additionally, ground-based telescopes cannot always monitor Venus temperatures. Because Venus is apparently too close to the sun at low or high phase angles, observations from the Earth generally have difficulty in covering all phase angles (i.e., local time). While the Texas Echelon Cross Echelle Spectrograph operated by the NASA Infra-Red telescope Facility (Lacy et al. 2002) has provided data covering various local times, there exist temporal gaps up to 2 years in their observations due to limited occasions (Encrenaz et al. 2012, 2016, 2020, 2023).

An alternative approach to address the gaps in monitoring datasets could be the utilization of meteorological satellites. Recently, meteorological satellites started to be recognized as space telescopes that can provide infrared observations of solar system bodies and stars. Although meteorological satellites are primarily designed for the Earth's weather observation, their imaging range simultaneously includes space adjacent to the Earth, occasionally capturing the Moon, planets, and stars. Such images of celestial bodies have been utilized in various ways in planetary science and astronomy. For instance,

Müller et al. (2021) benchmarked their thermal model in comparison with lunar images taken by the NOAA and MetOp satellites. Nishiyama et al. (2022) succeeded in retrieving lunar geologic information, such as roughness and rock abundance distribution, by analyzing lunar infrared images taken by the Advanced Himawari Imager (AHI) onboard the Japanese meteorological satellite Himawari-8. This satellite has also been used to monitor the great dimming of the red supergiant star Betelgeuse, providing insights into the mechanisms responsible for the phenomenon (Taniguchi et al. 2022). In addition, other planetary bodies, including Mercury, Venus, Mars, and Jupiter, have been captured by various meteorological satellites (Nishiyama et al. 2022; Fulbright et al. 2023; Burgdorf and Taniguchi 2024). As shown in Fig. 1, Venus has been taken by Himawari-8 at various phase angles until the present. Although the image resolution differs among wavelengths due to detector characteristics (Okuyama et al. 2018), these images demonstrate the potential of this satellite to contribute to Venus monitoring.

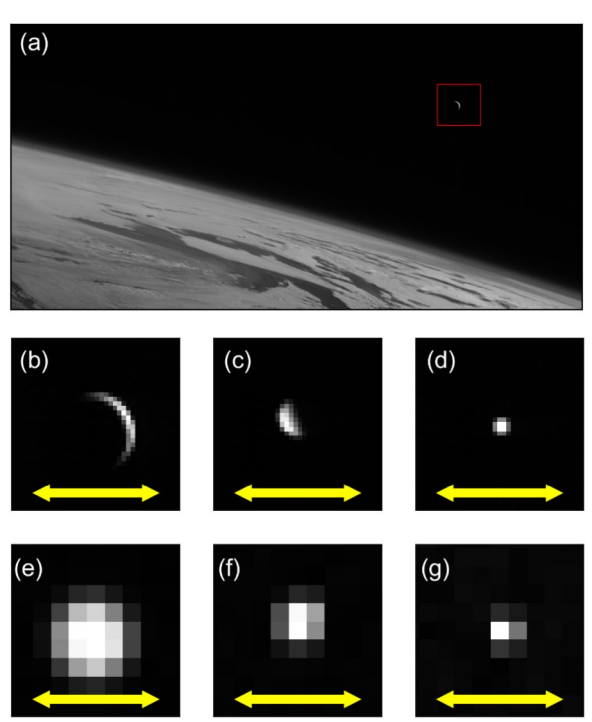


Fig. 1 Examples of the Venus observations by AHI at various phase angles. **a** Venus captured in space adjacent to the Earth. The lower left portion of the image shows the Earth. The red square highlights the area zoomed in **b**. **b**, **c**, **d** Venus images taken at band 3 (0.64 μm). **e**, **f**, **g** Venus images at band 10 (7.3 μm). **b**, **e**, **c**, **f**, and **d**, **g** show observations on 2023/07/23 at 16:40, 2023/10/24 at 11:00, and 2024/03/30 at 13:00, with phase angles of 139.1, 89.6, and 24.0 degrees, respectively. The yellow arrows indicate a scale of 1 arcminute

Frequent calibration of imagers onboard meteorological satellites is a major advantage for their application to planet observations. Among the most frequently calibrated infrared imagers is the Advanced Himawari Imager (AHI) onboard both the Himawari-8 and Himawari-9 satellites. Himawari-8 had been operated by the Japan Meteorological Agency (JMA) for 7 years until it turned into a stand-by status in December 2022. As its successor, Himawari-9 is currently conducting meteorological observations with an observation overlap with Himawari-8 approximately for a month. Both satellites are equipped with nearly identical AHIs and acquire fulldisk imagery of the Earth at 10-min intervals (Okuyama et al. 2018). During every imaging operation, the AHI is calibrated with cold space and an internal temperaturecontrolled heater (Griffith 2015). Due to the low noise levels of the AHI detectors, the noise-equivalent differential temperature is expected to be less than 0.22 K at 300 K at all the infrared bands (Takahashi and Okuyama 2017; Okuyama et al. 2018). Okuyama et al. (2018) also report brightness temperature bias of 0.2 K or less; therefore, this high level of precision offers potential opportunities to detect even subtle temperature variations in the Venusian atmosphere, possibly down to a scale of 1 K.

Another significant feature of the AHIs for planetary science is multiband coverage at mid-infrared wavelengths. AHIs are equipped with 16 spectral bands in total: three visible (0.4–0.7 µm), four near-infrared (0.8–4 μm), and nine mid-infrared (6–14 μm) bands (Okuyama et al. 2018; Fig. 2). Particularly at mid-infrared bands, spectrally resolved observations of Venus by planetary missions have been limited to specific timeframes. Since the Venera-15 observation in 1983 (Oertel et al. 1985), only the Mercury Radiometer and Thermal Infrared Spectrometer (MERTIS) onboard BepiColombo (Hiesinger and Helbert 2010; Hiesinger et al. 2020) had a measurement occasion during its Venus flyby in 2021 (Helbert et al. 2023). While the Akatsuki mission observed Venus at the mid-infrared wavelengths between 2015 and 2023, its long-wave infrared camera (LIR) has a single band and lacks spectral resolution (Fukuhara et al. 2011). Spectral resolution in the mid-infrared is essential for retrieving temperature information from different altitudes due to the strong dependence of Venusian cloud aerosol extinction coefficients at mid-infrared wavelengths (Pollack et al. 1993), as well as the overlapping absorption bands of atmospheric molecules like CO₂ (Fig. 2). The multiband capability of the AHIs could therefore offer valuable opportunities to fill gaps in altitude information that have been almost missing over the past decade.

These well-calibrated datasets are also beneficial for calibration of infrared cameras used in the Venus observations. Both Mercury and Venus have been considered

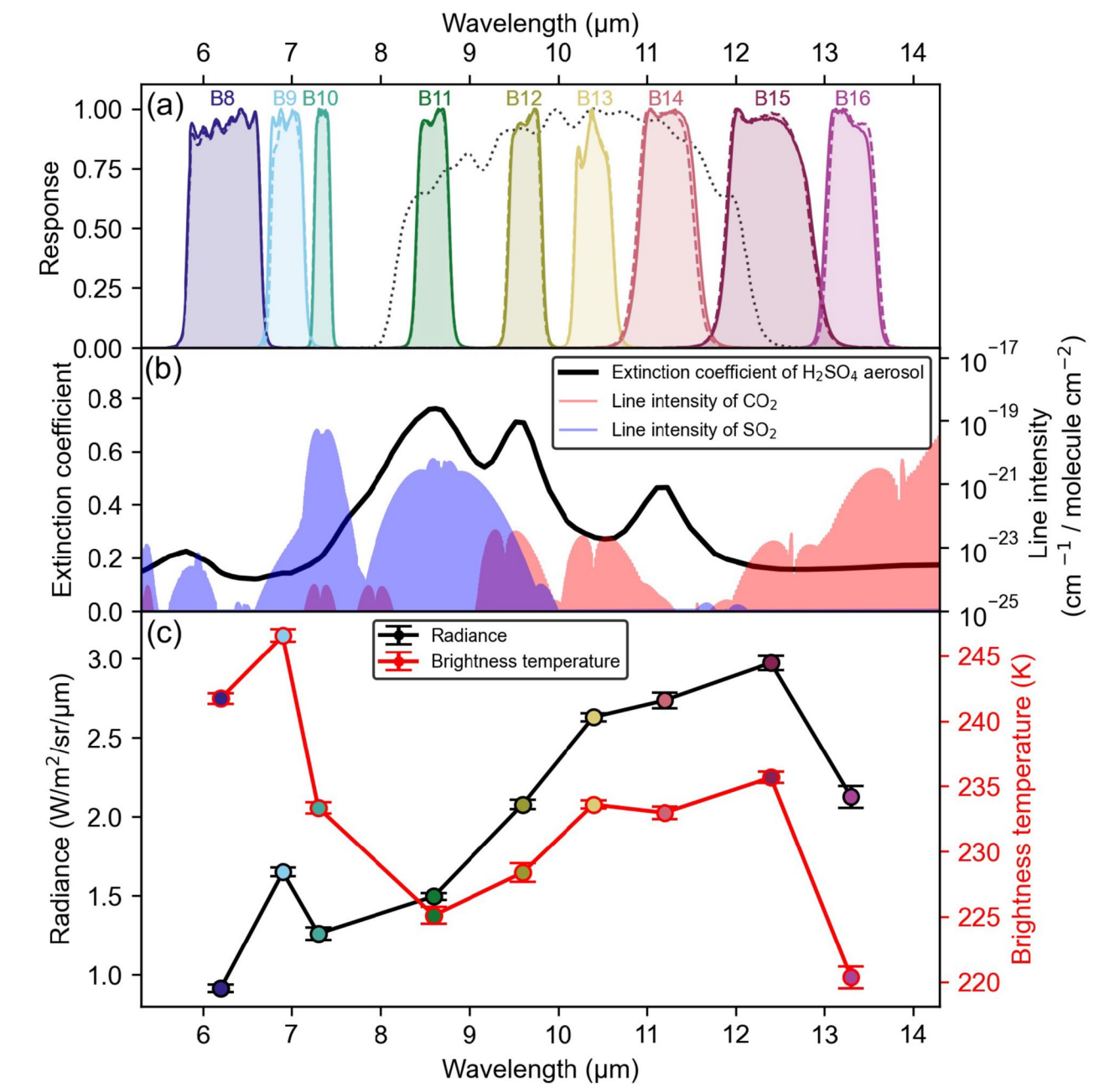


Fig. 2 Overview of the AHI observation. **a** Response functions of AHIs and LIR. The nine color shades represent responses of band 8 to 16 of AHI. The solid and dashed lines show the AHI response functions for Himawari-8 and 9, respectively. Note that the band numbers are sorted by their central wavelengths in ascending order. The LIR response function is shown as the dotted black line. **b** Spectral features of typical molecules and aerosol in the Venus atmosphere. The black line shows the extinction coefficient of the H₂SO₄ aerosol (Palmer and Williams 1975). The red and blue shades show the line intensities of CO₂ and SO₂, respectively, from the HITRAN2020 database (Gordon et al. 2022). **c** Example of a measured spectrum. Disk-integrated radiance and brightness temperature are shown in the black and red lines, respectively. The black and red error bars show the noise level in radiance and brightness temperature, respectively

potential calibration targets for meteorological satellites (Fulbright et al. 2023; Burgdorf and Taniguchi 2024). This calibration approach could be extended to planetary mission instruments, as Nishiyama et al. (2022)

demonstrated a comparison between AHI and the Diviner Radiometer onboard the Lunar Reconnaissance Orbiter (LRO). Given that the noise-equivalent temperature of AHI is 150 K or less at all the infrared bands, the

Venus images taken by AHI are precise enough to verify functionalities of other instruments at the typical Venus temperature of approximately 230 K. For instance, the Venus flyby of BepiColombo is a rare chance to validate the MERTIS calibration (D'Amore et al. 2018; Hiesinger et al. 2020). In addition, LIR has experienced calibration problems in orbit, such as unexpected bright signal due to thermal emission from its baffle heated by sunlight (corrected by Fukuhara et al. 2017) and long-term background temperature increase likely due to sensitivity degradation of its bolometer array (corrected by Taguchi et al. 2023). Although these effects have been corrected in the latest LIR dataset, a discrepancy in brightness temperature at 10 µm appears to remain between MER-TIS and LIR data during the BepiColombo Venus flyby. The temperature detected by LIR in Taguchi et al. (2023) is lower than that by MERTIS in Helbert et al. (2023) approximately by 5 K. These discrepancies could be more thoroughly investigated and resolved by integrating AHI data.

Aiming to investigate the temporal variation of the Venus atmospheric dynamic and to provide a comparative analysis with previous Venusian datasets, this study presents a new decadal-monitoring dataset of the Venus brightness temperature at infrared wavelengths. We first establish a data archive by extracting all the Venus images from the entire AHI datasets. The archived radiance data are then compared with the LIR and MERTIS observations, considering differences in observation geometries and response functions among the three instruments. Retrieved temporal variations in brightness temperatures are next analyzed on both year- and day-scales and compared among all the infrared bands to investigate variability of thermal tides and planetary-scale waves. Finally, we discuss possible factors of the observed variations and future potential of AHIs for Venus science. Note that this study focuses on Himawari-8 and -9 satellites since their imagers have the highest temporal and spatial resolutions among existing meteorological satellites that observe the full-disk Earth frequently.

2 Venus radiance archived from the AHI data

Using Himawari Standard Data (HSD) that the Japan Meteorological Agency (JMA) has published (Japan Meteorological Agency 2017), we archived all the Venus images captured by AHI at each infrared band and derived disk-integrated radiance. Particularly, data at band 8–16, covering 6–14 μ m, are featured in this study because reflection of sunlight is the major contributor to the measured radiance at the other bands. After identification of the Venus position in each HSD, the aperture-photometry technique was applied to calculate disk-integrated radiance, following Nishiyama et al.

(2022) and Taniguchi et al. (2022). As background level in space is dependent on apparent distance from the Earth likely due to stray light (Nishiyama et al. 2022; Taniguchi et al. 2022), the background radiance was estimated from the surrounding pixels and subtracted from the radiance inside the aperture before deriving the disk-integrated radiance. Figure 2 shows an example of disk-integrated radiance and the corresponding brightness temperature derived from this photometric procedure. Figure 2 clearly depicts the brightness temperature dependency on the $\rm H_2SO_4$ aerosol and $\rm CO_2$ spectral features because of their effect on sensing altitudes (described in detail in Sect. 4). Details of the retrieval methodology can be found in Appendix.

After surveying all the HSD taken until February 2025, we identified 437 occurrences of Venus in AHI images. It should be noted that the Venus images are occasionally missing at some bands when Venus is near the scanning boundaries because the published scanning areas differ slightly among the bands. In addition, the Venus radiance may be contaminated by the terrestrial atmosphere and stray light when it is close to the Earth in the image. Although these effects were corrected through the background subtraction, the latter analyses are conservatively limited to cases where the background radiance is less than 10% of the Venus signal. It is noteworthy that the coverage of phase angles is extensive, ranging from 3 to 174 degrees. AHI is capable of observing Venus as long as the Sun is hidden by the Earth, enabling measurements even when Venus appears close to the Sun. Consequently, the AHI observations span almost all the local times (Fig. 3a). The local time of the AHI observation is defined at the disk center of Venus (i.e., the sub-Himawari points on Venus).

The derived radiance may contain errors due to the background noise and effects of Venus's apparent size. While the noise level is expected to be as low as 0.22 K based on prelaunch ground testing (Takahashi and Okuyama 2017; Okuyama et al. 2018), the impact of Venus's apparent size may be more significant. During the data reduction, as the original image is converted into HSD by JMA, detector samples are weighted and resampled onto a fixed coordinate grid (Kalluri et al. 2018). This reduction process may cause additional errors, particularly when Venus is at its furthest point from the Earth. In such cases, sensitivity variations within individual detector elements might affect the radiance measurement because its apparent diameter becomes identical to the instantaneous field of view of the AHI detector (Griffith 2015).

To estimate the actual observation error, we compared two Venus images that were coincidentally taken on the same day. Because it takes 1 h at maximum for

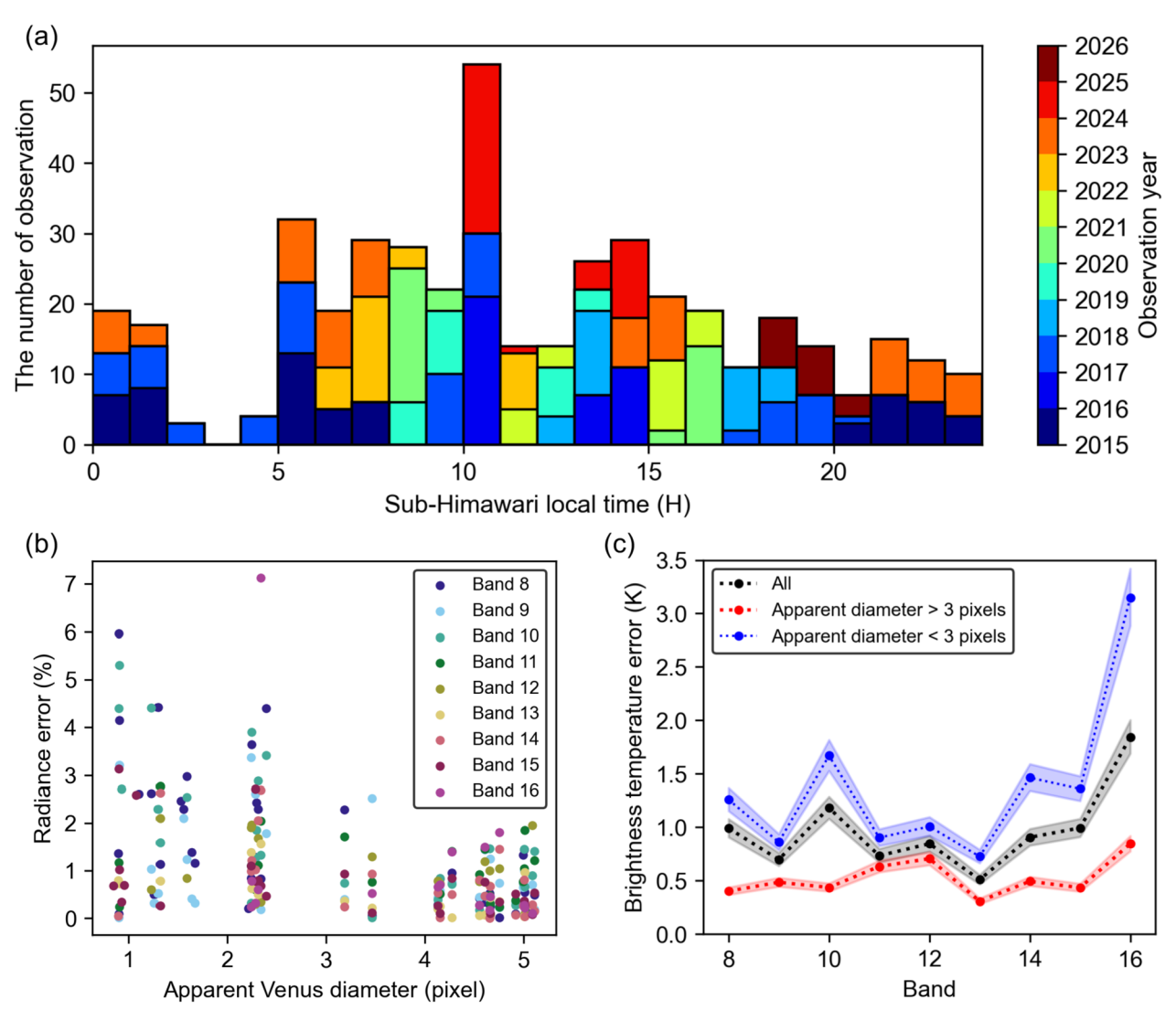


Fig. 3 Summary of observation geometry by AHI. **a** Histogram of local time coverage on Venus. The colors of the histogram correspond to the observation year. **b** Observation errors in radiance ratio estimated from the same date observations. **c** Observation errors in brightness temperatures at each infrared band. The dashed lines correspond to the errors at the reference temperature of 230 K. The shades show ranges of the errors at the reference temperature from 220 to 240 K. The black plots show the RMS of all the observation errors. The red and blue plots show the RMS values when the apparent Venus diameter is larger and smaller than 3 pixels, respectively

Venus to pass from the left to right edge in the AHI scanning area, the AHI observation at every 10 min is frequent enough to occasionally capture Venus on both the left and right of the Earth within the same day. Note that the apparent diameter of Venus is identical between these two observations because the distance between Venus and AHI does not change in the short time interval. From the archived dataset, we identified 63 events where Venus was imaged twice in a day, with time intervals ranging from 20 to 60 min. Given that the radiance of Venus does not change over such short timescales, the differences in radiance between two

consecutive observations can be treated as observation errors.

Figure 3b shows these differences as ratios to the average of the two observations. The error decreases with the captured Venus size in the AHI images due to the apparent size effect. The root-mean-square (RMS) of the radiance error is converted to brightness temperature at different reference temperatures (Fig. 3c). At a reference temperature of 230 K, the average error in brightness temperature is less than 1 K. Although the error level depends on the reference temperatures due to the non-linearity of thermal emission, the change is minimal

when typical temperatures of 220–240 K are considered as the reference (color shades in Fig. 3c). When the apparent size exceeds 3 pixels, the error consistently falls below 0.85 K, ensuring that even 1 K variation is detectable in the latter analyses.

The error analysis confirms that AHI is capable of tracking temporal variation in the Venus temperature. Figure 4 provides an overview of all the Venus observations made by AHI. Because the geostationary orbits of Himawari-8 and 9 are not parallel with the Venus revolution orbit around the sun, AHIs could not always capture Venus until the present. Consequently, the archived data consist of 23 distinct periods, each lasting up to two months. Despite gaps in certain timeframes, year-scale temperature variations are resolved and exceed the estimated error levels at all the bands. Moreover, day-scale variations are trackable within two periods whose observation intervals can be down to a day (see Sect. 4.2).

3 Comparison among AHI, LIR, and MERTIS

To validate infrared remote-sensing data of Venus from planetary missions, comparisons among AHI, LIR, and MERTIS were conducted. Due to differences in observation geometry, comparisons among AHI, LIR, and MERTIS cannot be performed directly. The spatial and temporal coverage of the observations must be carefully considered, as Venus's atmospheric temperature is highly dependent on time, latitude, and local time (e.g., Seiff et al. 1985; Zasova et al. 2006; Kouyama et al. 2019; Kajiwara et al. 2021). In addition, the spatial resolution

of Venus is significantly different among the three: AHI obtains only disk-integrated radiances, whereas LIR and MERTIS obtained spatially resolved radiances (Fig. 5a). Furthermore, the emission angle is another important factor because the cloud layer may cause almost a 5-km difference in sensing altitude among emission angles (Akiba et al. 2021). According to the Venus International Reference Atmosphere (VIRA) model (Seiff et al. 1985), this altitude variation can result in temperature differences of 10 K. Therefore, to ensure valid comparisons under identical conditions, the focus is on two specific sets of data: disk-integrated radiance comparisons between AHI and LIR, and local radiance comparisons between LIR and MERTIS.

Another factor that complicates direct comparison is a difference in spectral coverage among the three instruments. Although AHI, LIR, and MERTIS observe similar wavelength ranges, their spectral resolutions are significantly different. AHI and LIR have nine and single response functions, respectively, with bandwidths larger than 0.2 µm (Fig. 2a; Fukuhara et al. 2011; Okuyama et al. 2018). In contrast, MERTIS offers higher spectral resolution, covering 7-14 µm with 78 spectral channels and achieving a spectral resolution of 0.090 µm (Hiesinger et al. 2020). When we compare two of the three instruments, the dataset from the instrument with higher spectral resolution is convolved with the response functions of the other. Namely, the MERTIS dataset is weighted and summed using the response functions of LIR for comparison. When AHI was compared with LIR, the product of

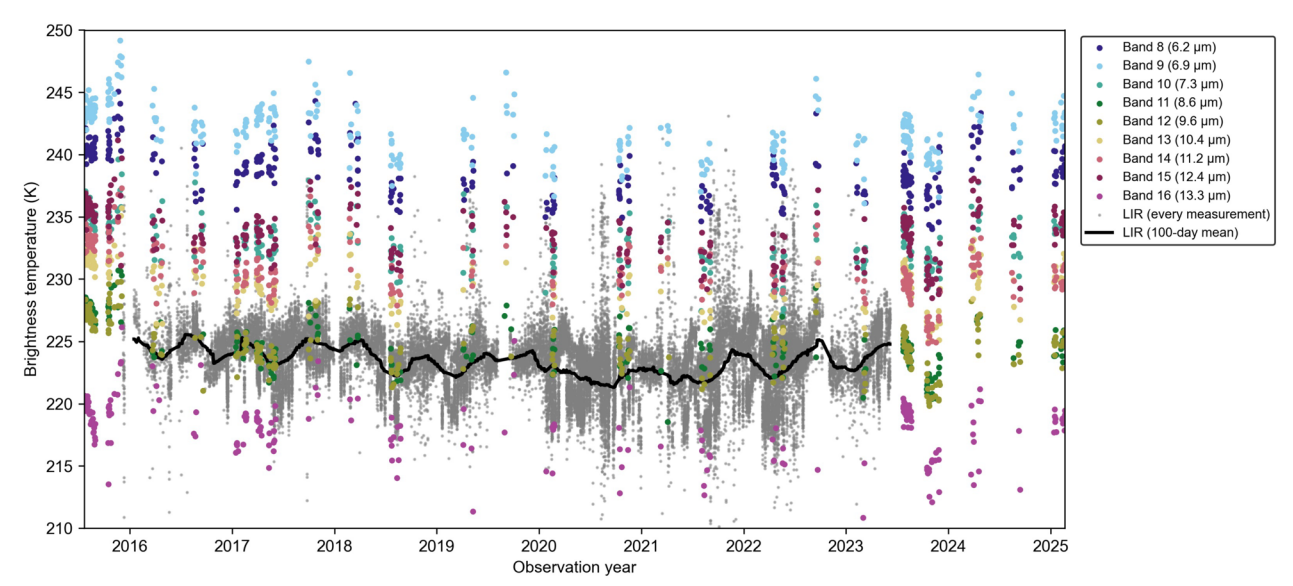


Fig. 4 Overview of all the measured Venus temperature. The colors of dots correspond to the AHI band number, following the same definitions as in Fig. 2a. The gray points represent all the LIR observations when entire Venus is captured within a single image. The black line shows running mean values with a window of 100 days, calculated at step size of 1 day

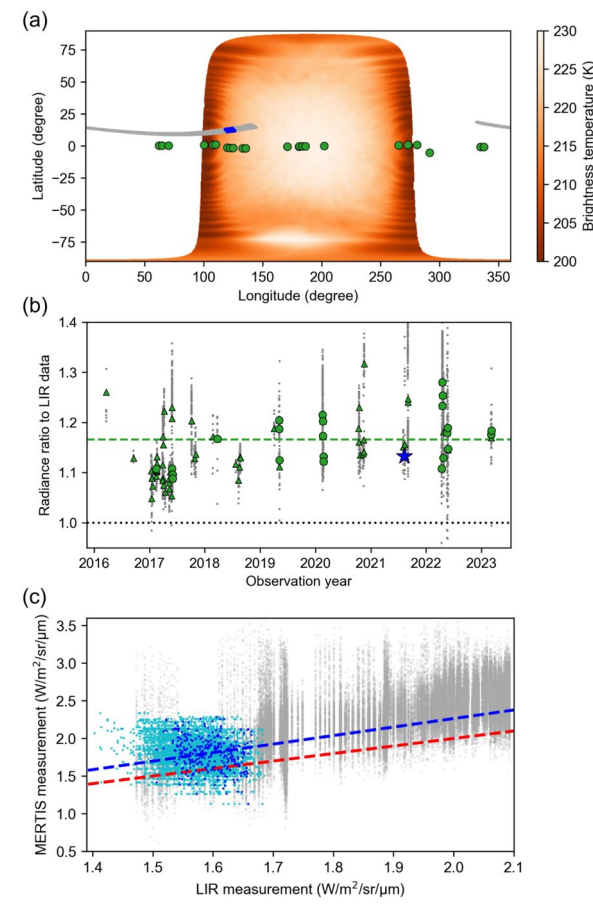


Fig. 5 Summary of comparison among AHI, LIR, and MERTIS. a Footprint locations of the three instruments. The gray scatters show all the MERTIS footprints during the flyby. The blue points are the MERTIS footprints whose observation geometries are identical to LIR. The LIR brightness temperature data (20210810_140112) are shown as a background color map. The green points are sub-Himawari points of the AHI observations when the difference in local time at sub-spacecraft points between Akatsuki and Himawari-8/9 is smaller than 1 h. While the absolute value of local time differences is used for the criterion, it should be noted that no systematic bias in local time is confirmed by checking the distribution of differences. **b** Radiance ratio of AHI and MERTIS to LIR observations. The gray dots are ratios of the AHI data to all the LIR data taken within a one-day gap. The green dots show the average of the gray dots for each AHI observation. The green dots and triangles correspond to results with local-time differences of smaller and larger than 1 h, respectively. The blue star shows the average ratio of the MERTIS data to the LIR. c Radiances measured by MERTIS and LIR under similar conditions. The blue and cyan points are data when the longitude, latitude, and emission angle of the MERTIS pixels match those in the LIR data taken at 14:01 and other time on 10 August 2021, respectively. The gray points are comparison results when only latitude and emission angles match in both data. The red dashed line indicates the case where the radiance values from both MERTIS and LIR are identical. The blue dashed line indicates the case where the radiance measurements of MERTIS are higher than those of LIR by 15%. Note that all the observations of MERTIS and AHI on b and c are convolved with the LIR response function

the AHI and LIR response functions was used as weighting coefficients for the convolution. This approach might introduce a systematic error because the AHI bands do not fully cover wavelengths of the LIR response function. However, testing with the MERTIS hyperspectral data confirmed that this method introduces only a minor artifact, with an error of 2% or less. The details of our spectral convolution method for AHI-LIR and MERTIS-LIR comparisons are summarized in Appendix.

The comparison between AHI and LIR reveals a discrepancy in the radiance measurements with LIR yielding lower values than AHI. The LIR data used for the comparison were taken from the L3d products of the PDS4 Akatsuki LIR Bundle, which were the latest data after correction of the sensitivity degradation correction (Taguchi et al. 2023). For comparison with AHI, diskintegrated radiance was calculated by summing all pixel values of LIR images where the entirety of Venus was captured. In Fig. 4, while temporal variations detected by AHI and LIR are similar with a correlation coefficient of 0.55, there is a non-negligible offset in the observed temperatures between AHI and LIR. For example, band 13 of AHI, whose response function covers 10 µm as well as LIR, shows brightness temperature constantly higher than LIR by 5 K.

Figure 5b illustrates this offset in radiance ratio by normalizing the AHI radiance with the LIR one on the same date. In total, we found 72 AHI observations whose observation time matches at least one LIR observation within a day. 23 of those have less than a 30-degree longitudinal difference in location. Because the LIR data have a variation in radiance even within a day, the AHI measurement is compared with the average of the LIR measurements conducted on the same day. When comparing observations with nearly identical geometries, AHI consistently yields radiances that are on average 17% higher than LIR (Fig. 5b). Although both instruments are operated at different distances from Venus, the observed radiance discrepancy cannot be attributed to geometric effects. The difference in distance of instruments to Venus accounts for less than a 1% variation in radiance. In addition, the effect of the pixel field of view cannot account for the difference because this comparison includes data when Venus is at the maximum size of 5 pixels in the AHI images. Instead, it likely stems from intrinsic differences in functionalities and calibrations of the instruments.

A similar offset is also obtained in the comparison between LIR and MERTIS, even after careful selection of data points under identical observation conditions. The MERTIS observations on 10 August 2021 were limited to a region at latitudes of 8–19° N and local times of 6–18 h due to the close distance to Venus (Helbert et al.

2023). Coincidentally, LIR took 15 Venus images on the same day, one of which was taken within the duration of the MERTIS observations and partly covered footprint locations of the MERTIS measurements (Fig. 5a). This spatial and temporal overlap between LIR and MERTIS footprints, with identical emission angles, allowed for a direct comparison between the two datasets. As shown in Fig. 5c, the comparison indicates a consistent trend: radiance values measured by MERTIS are, on average, 15% higher than those measured by LIR. Particularly, the blue scatters in Fig. 5c correspond to data points whose emission angle, latitude, and longitude overlap within 5 degrees. Other LIR observations on 10 August 2021 also show a similar difference between the two (cyan scatters in Fig. 5c). This trend persists even when only emission angle and latitude are comparable, without strict longitude matching (gray scatters in Fig. 5c). This consistency across various comparison criteria implies that the radiance discrepancies are not due to observational geometry but likely arise from calibration differences between LIR and MERTIS.

These two comparison results suggest that LIR has likely underestimated the Venus radiance by 15-17%. This discrepancy is unlikely to originate from AHI, as its data show less than a 0.2 K bias compared to other Earthobserving instruments (Okuyama et al. 2018), and resampling errors during data processing are insufficient to explain the difference. The fact that MERTIS also shows a similar offset in comparison with LIR further points to the likelihood that the issue lies with LIR's calibration. LIR has experienced multiple calibration problems since its orbit insertion, such as unexpected dependencies on the LIR baffle temperature (Fukuhara et al. 2017) and temporal variations in background deep-space temperature (Taguchi et al. 2023). However, the 15-17% underestimation identified in this study implies an additional unresolved calibration issue within the LIR dataset. Although the root cause of these discrepancies is not clear at present, future analyses of LIR data need to take this underestimation into account until further recalibration for LIR is made.

In contrast, these comparison results suggest robustness of the laboratory-based calibration of MERTIS. Hyperspectral observation of the Venus temperature is known to be a challenging operation for MERTIS (Helbert et al. 2023). Since MERTIS was designed primarily for Mercury, where surface temperature can reach up to 700 K (Hiesinger et al. 2020), the Venus cloud-top temperature of around 230 K is near the lower detection limit of the infrared grating spectrometer (TIS) of MERTIS. However, the observed radiance discrepancy of only a few percent, when indirectly compared with AHI via LIR data (Fig. 5b), supports the reliability of

the MERTIS calibration. MERTIS is calibrated with two internal blackbodies and cold deep space, based on spectral sensitivity characterized through laboratory experiments conducted under thermal-vacuum conditions like space (D'Amore et al. 2018). While one of the blackbodies exhibited temperatures higher than Venus during the Venus flyby (Helbert et al. 2023), the small discrepancy implies that temperatures as low as 230 K can still be detected accurately at mid-infrared wavelengths after stacking noisy spectra. Thus, despite Venus being outside the primary design focus of MERTIS, these results confirm the instrument functionality even for the terminator region on Mercury, where surface temperatures can be similarly low (e.g., Bauch et al. 2021).

4 Temporal variation of Venus temperature structure

As shown in Fig. 4, the Himawari data can observe the temporal variation of the Venus temperature at various time scales. In this section, we analyze the archived data from two perspectives: thermal tide stability over years and altitude dependency of planetary-scale waves. Since LIR perhaps has a calibration problem (Sect. 3), the AHI data offer an independent opportunity to investigate these phenomena. The multiband measurement by AHI might additionally provide valuable insights into the vertical structure of Venus's atmospheric dynamics.

Prior to retrieval of altitude information from the AHI multiband measurements, it is essential to calculate the weighting function at each AHI band. The weighting functions represent the altitude-dependent contributions to the observed radiance at different wavelengths, showing which atmospheric layers are being sensed by various AHI bands. To compute the weighting functions, the Planetary Spectral Generator (PSG) was employed to model the radiative transfer within the Venus atmosphere (Villanueva et al. 2018), incorporating the cloud aerosol distribution and temperature profile. Based on the cloud model developed by Haus et al. (2013), four modal distributions of H₂SO₄ aerosols are considered in our calculations. Log-normal size distributions are assumed with modal radii of 0.3, 1.0, 1.4, and 3.65 μm (Pollack et al. 1993; Helbert et al. 2023). For the refractive index of particles, the PSG model considers data from Palmer and Williams (1975). The effect of emission angle is incorporated in these PSG calculations by considering distribution of emission angles inside a full disk of Venus. The temperature profile was based on the VIRA model for latitude of 30 degrees (Seiff et al. 1985). Note that the altitude order of the bands does not change even if the temperature profile of the VIRA model for other latitudes is used in the calculation.

Figure 6 shows the weighting functions of all the infrared bands of Himawari 8 and 9. The mean values of weighting functions, including LIR, are summarized in Table 1. The weighting functions of bands 8 to 15 are influenced primarily by the wavelength-dependent refractive index of the H₂SO₄ aerosol, mainly sensing altitudes below 70 km. On the other hand, because of strong absorptions by CO2 above the cloud, the weighting function of band 16 ranges widely from 60 to 83 km in altitude. Therefore, observations at band 16 provide the highest-altitude information among the AHI bands. These results demonstrate that the AHI multiband observation is capable of sensing temperature structure at altitudes from 60 to 70 km. Note that differences in weighting functions between Himawari 8 and 9 are minimal due to their nearly identical response functions, although the difference at band 16 appears larger than those at other bands due to drastic variation in sensing altitude at band 16 due to the CO₂ absorption.

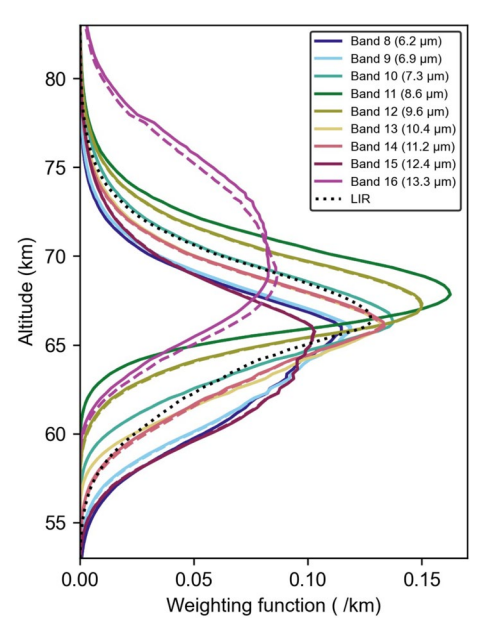


Fig. 6 Weighting functions at all the AHI infrared bands. The black dashed lines show the weighting function of LIR. The other colored dashed and solid lines show the weighting functions at each AHI band of Himawari-8 and 9, respectively

4.1 Year scale: thermal tide structure

The temporal variability of the thermal tide pattern is not fully understood; however, it is important for deciphering long-term atmospheric dynamics. Previous observations have shown that the global structure of the thermal tides is composed of diurnal and semi-diurnal tides with two local maxima of temperature around 9 and 19 h in local time (e.g., Kouyama et al. 2019). According to numerical simulations of the temperature field (Takagi and Matsuda 2005; Suzuki et al. 2022), the diurnal tides are highly sensitive to various factors, including the midlatitudinal jets, Newtonian cooling rates, and static stability. In addition, variations in albedo may contribute to the thermal tides through their excitation. A decadal-scale variation of the global albedo has been revealed by combining previous measurements (Lee et al. 2019), though initial analyses of the LIR data for the first three years show little variations in the thermal tide structure (Kouyama et al. 2019). Based on consistency with previous observations, they suggest a steadiness of the structure over the years. However, this structure steadiness over a longer time scale remains an open question as analysis of the LIR data by Lai and Li (2023) indicates an unstable structure of thermal tides.

Although AHI provides only the disk-integrated radiance of Venus, the thermal tide structure is captured well at all the bands. Figure 7 depicts the brightness temperatures at various local times at each band. The brightness temperature variation has a similar pattern dependent on local times at all the bands. The brightness temperature around midnight decreases with local time (the black arrows in Fig. 7). The local minimum and maximum exist at local times of approximately 16 h and 20 h, respectively. These features are qualitatively consistent with the thermal tide patterns observed by LIR (Kouyama et al. 2019; Akiba et al. 2021). Note that the semi-diurnal tide is observable in the AHI measurements while this structure can be averaged to some extent due to the hemispheric coverage. The disk-integrated radiance is more sensitive to emission from the disk center due to the emission angle effect, which prevents smoothing out the semi-diurnal component.

In contrast, the AHI observations reveal a significant temporal variation in brightness temperature from 2015 to the present, particularly on the morning side of Venus (Fig. 7). For example, the measurements in 2015

Table 1 Mean altitudes of the weighting function at each band. The unit is km

	Band8	Band9	Band10	Band11	Band12	Band13	Band14	Band15	Band16
Himawari 8	64.7	65.0	67.1	68.9	68.1	66.3	66.1	64.9	70.8
Himawari 9	64.7	65.1	67.1	68.9	68.2	66.3	66.2	64.9	71.2
LIR	66.6								

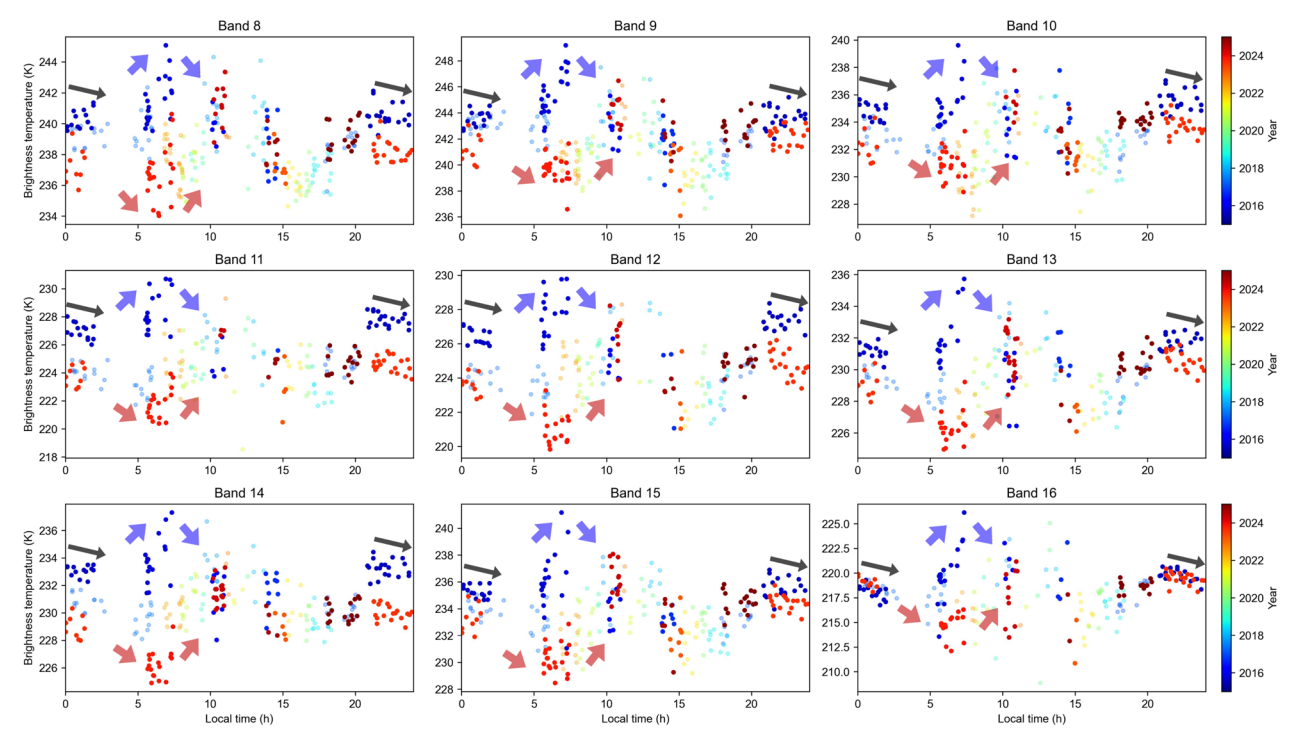


Fig. 7 Brightness temperatures measured at each band and local time. The colors of dots correspond to observation years. The color transparency of observations between 2015–2016 and 2023–2025 is decreased to emphasize temporal variation observed in this study. The arrows show variations at the midnight and morning sides

show a temperature decrease with local time from 21 to 2 h, followed by an increase from 5 to 7 h in local time, respectively. This trend indicates the temperature minimum around the local time of 3-4 h, consistent with the semi-diurnal component of the thermal tides. On the other hand, the temperature minimum on the morning side shifts to around the local time of 6 h in 2023, consistent with the diurnal component of the thermal tides. Such large temporal variations in brightness temperature are mainly observed around sunrise. Figure 8 shows the temporal temperature variation at local times of 0, 6, 10, and 17 h, where brightness temperatures are measured in multiple periods within a 1-h local-time window at every band. The mean temperature at the same local time was subtracted to emphasize temporal variation. At all the bands, the most pronounced year-scale variation over the past decade is observed at a local time of 6 h.

Figure 8 also reveals an altitude dependence of the year-scale variation in brightness temperature within the same local time. At bands 8 to 15, the temporal variation displays a similar pattern at each local time; however, band 16 shows distinct temporal variations compared with the other bands. For instance, the midnight temperature measured in 2015, 2017, and 2023 constantly decreases with year at band 8 to 15, while an increase with time is observed at band 16. At a local time of 10 h, only band 16

has the temperature minimum in 2023, while the other bands rather exhibit the highest temperature values. As demonstrated by the weighting functions in Fig. 6, band 16 captures altitude information substantially different from the other bands. Therefore, the multiband measurement by AHI indicates that the year-scale variation in temperature at altitudes above 70 km may occasionally contrast with those at lower altitudes.

These temporal variations may be interpreted as a change in diurnal tides. The higher brightness temperature of the morning side in 2015–2016 compared to later time is consistent with enhancement of diurnal tides in 2023-2025. Because the diurnal tide has the minimum temperature deviation at sunrise, enhanced diurnal tides can decrease the temperature in the morning, indicated by the red arrows in Fig. 7. In contrast, observations in 2015-2016 have semi-diurnal patterns rather than diurnal ones as the highest temperature is observed in the morning (the blue arrows in Fig. 7). The difference in temporal change patterns between band 16 and the other bands (Fig. 8) might also be correlated with diurnal tides. A previous numerical simulation suggests a change in phase of diurnal temperature deviations at 73 km (e.g., Suzuki et al. 2022), which is located inside the range of sensing altitudes of band 16. While the AHI observations are too sparse in time to infer duration of enhancement

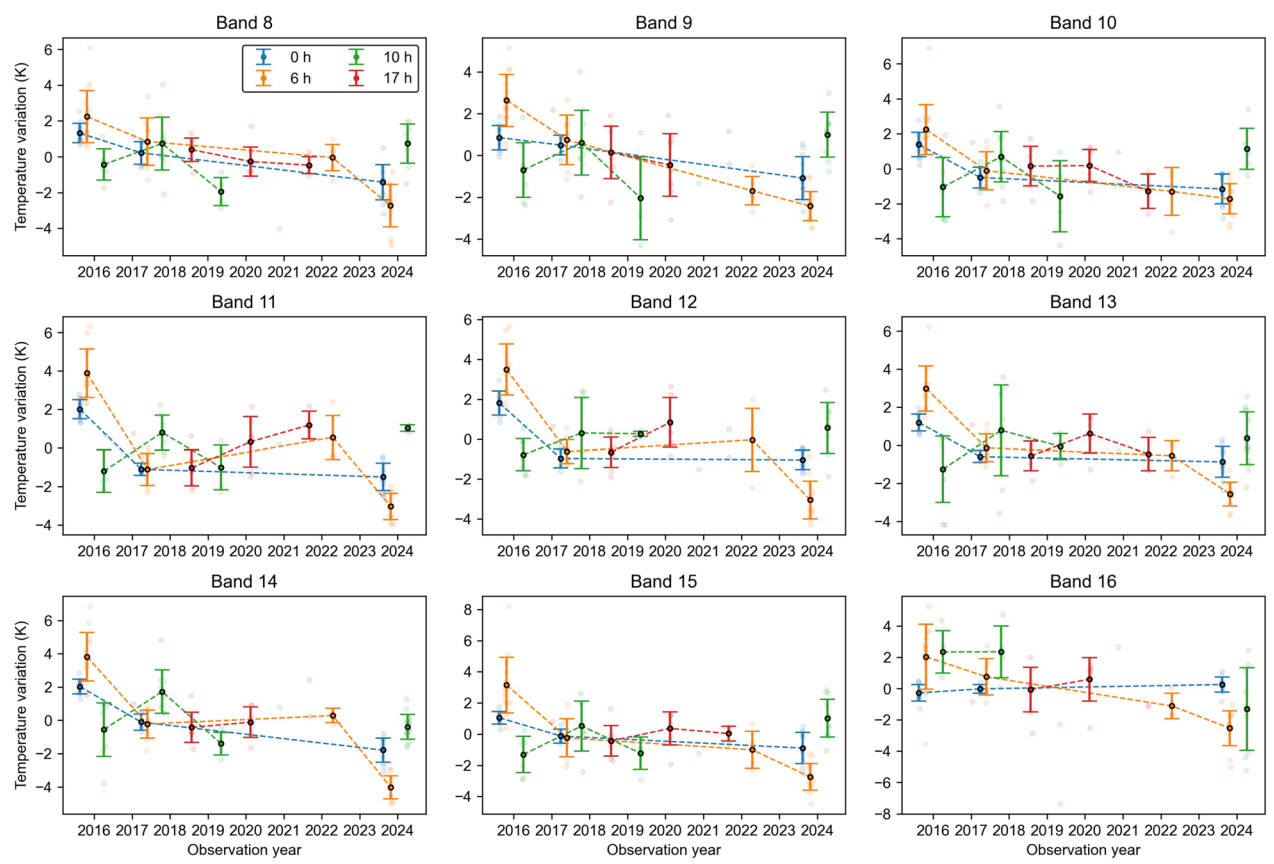


Fig. 8 Brightness temperature variation within the same local time for each band. The transparent dots show each AHI observation point. The black-framed dots and error bars show the mean and standard deviation of the data for observation periods with more than three successful measurements. The blue, orange, green, and red correspond to local times of 0, 6, 10, and 17 h, respectively. Note that the averages of brightness temperatures are subtracted to visualize the temporal variation in temperature

of diurnal components, future analysis of thermal tide patterns with the LIR data may be correlated with the observed results.

4.2 Day scale: Rossby wave structure

The altitudinal structure of planetary-scale waves can also be investigated by frequent observations over time. As observed in the UV reflectance and temperature field, the planetary-scale waves are composed of Rossby and Kelvin waves with circulation periods ranging from 3 to 6 days (Del Genio and Rossow 1990; Kouyama et al. 2013, 2015; Imai et al. 2019; Nara et al. 2019; Kajiwara et al. 2021; Lai and Li 2023; Horinouchi et al. 2024). AHI can capture Venus as often as once a day, depending on observation conditions, and hence, can resolve these dayscale variations particularly when the noise levels are low. Moreover, the multiband measurements of AHI may allow for the detection of differences in the amplitude of planetary-scale waves at various altitudes. Although multiple numerical simulations have predicted an altitude dependency of amplitude in temperature (e.g., Kouyama et al. 2015; Takagi et al. 2022), such altitude dependency has not been observed directly in the temperature field yet.

Such an altitudinal dependence was observed in two AHI measurement periods: 2015/07/21-08/29 and 2023/07/23-08/22 (Fig. 9a and c). During these two observation periods, AHI was able to continuously capture Venus with apparent sizes of up to 5 pixels, which reduces the noise level to less than 1 K (Fig. 3c). Unfortunately, observations during the other periods were either too scarce or too noisy to support a meaningful analysis of day-scale periodic behaviors. In Fig. 9a and c, the brightness temperature variations appear similar between low-altitude bands, such as bands 8 and 9. However, this similarity diminishes with increasing sensing altitude. After detrending the long-term temperature variation in 2015/07/21-08/29, the correlation coefficients with band 8 were found to be 0.80, 0.37, and 0.06, for band 9, 11, and 16, respectively. A similar trend is observed in 2023/07/23-08/22 with correlation coefficients of 0.82, 0.50, and 0.33.

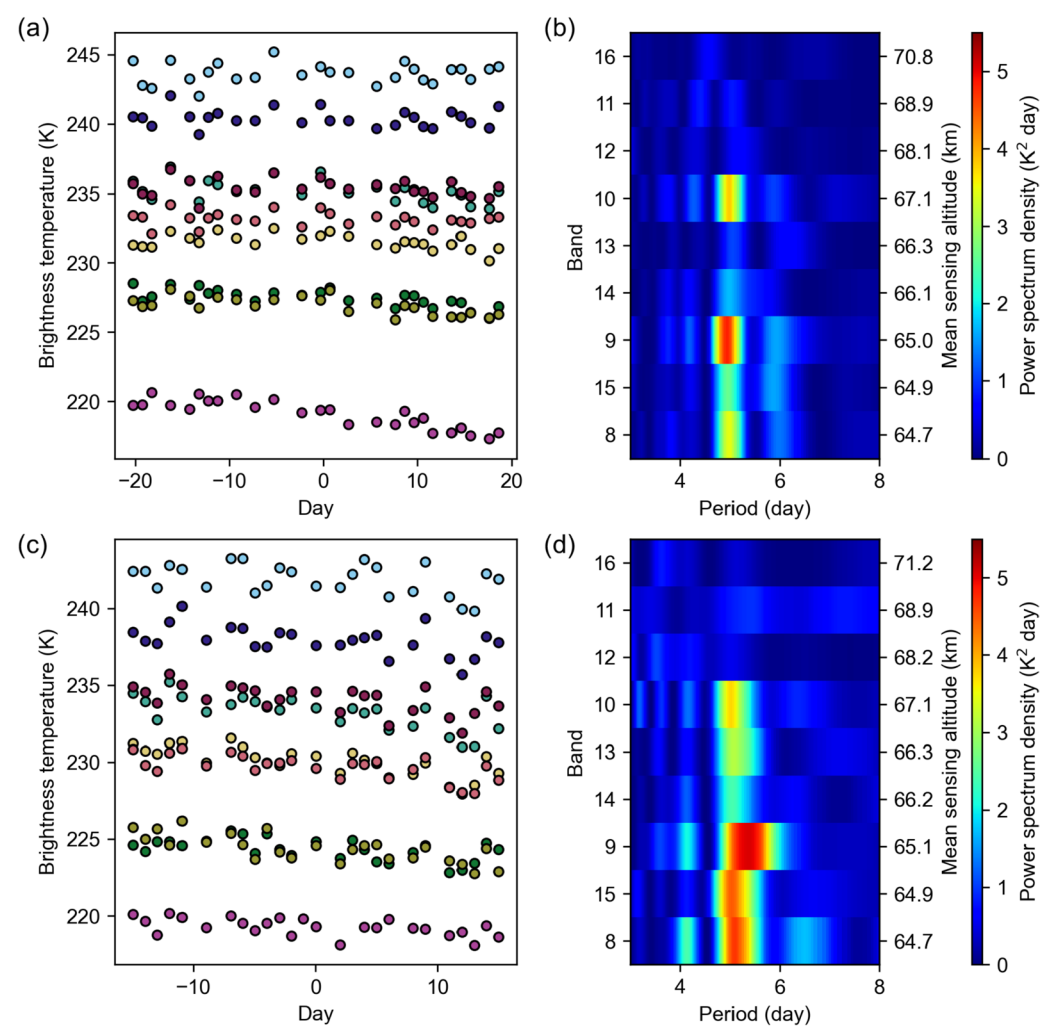


Fig. 9 Day-scale variations observed at two periods. **a, b** 2015/07/21–08/29; **c, d** 2023/07/23–08/22. **a, c** Brightness temperature at each infrared band. The x-axis shows the time in day from the center of each period. The colors of dots correspond to the AHI band number, following the same definitions as in Fig. 2a. **b, d** Lomb–Scargle periodogram applied to the brightness temperature sequences in **a** and **c**. The band numbers in the y-axis are ordered by the mean altitudes of the weighting functions (Table 1). The corresponding mean sensing altitude is labeled in the right y-axis

To unravel the altitude dependency in terms of periodicity, we applied the Lomb–Scargle periodogram to the two measurement periods. While the sampling interval during the observations is almost a day, it is not entirely uniform due to several missing data points. Thus, the periodicity of the brightness temperature variation is analyzed with the Lomb–Scargle periodogram (Scargle 1982), which is commonly applied to data with uneven sampling. Temperature decreases on time scales longer than the observation periods are attributable to thermal tides as this decreasing trend with increasing local time around midnight is known as the thermal tide pattern from previous studies (Kouyama et al. 2019). These decreasing trends were removed by fitting a linear

function before the periodicity analysis. Although the data gap could affect the analysis result, the Lomb–Scargle periodogram was also applied to artificial sinusoidal variation sampled at the actual observation time to validate our analysis method in the latter analyses.

The application of the Lomb-Scargle periodogram revealed a notable decrease in the amplitude of the 5-day period wave with increasing altitude, particularly above 68 km. Figure 9b and d show the Lomb-Scargle periodogram for both observation periods. Except for bands 11, 12, and 16, the largest amplitude occurs at the 5-day period, which corresponds to the Rossby wave. This feature is consistent with analysis of the LIR data by Kajiwara et al. (2021), who reported the maximum

amplitude in temperature at the 5-day period. As the second largest component, they also identified the 5.4-day Rossby wave, which may be unresolved from the 5-day wave because the minimum observation interval is one day in the AHI data. Furthermore, the AHI data indicate that the amplitude of the 5-day wave decreases with increasing altitude in both the observation periods. Figure 10 shows the amplitude in temperature at the 5-day period extracted from Fig. 9b and d. Note that the maximum amplitude between 4.5 and 5.5 day periods is used as the amplitude of the 5-day wave because it does not exist exactly at the 5-day period (Fig. 9b and d). The lowest amplitudes are observed at bands 11, 12, and 16, corresponding to altitudes above 68 km (Fig. 6; Table 1).

These altitude dependencies observed in both the observation periods are statistically validated through a Bayesian approach. Due to the influence of the observation error, the estimated amplitude might not necessarily reflect the true signal amplitude. To assess the actual amplitude in a statistical manner, we applied the Lomb-Scargle periodogram to artificial sinusoids synthesized with the measurement errors from Fig. 3b. In this Bayesian analysis, we maintained a constant period of 5 days for the sinusoid, while the sinusoidal amplitude is varied. To mimic the observations, the sampling times were also set to match those of the actual measurements. Based on these simulations, we estimated the probability of the true amplitude as illustrated in Fig. 10. While the probability distributions for the true values are broad for each observation, the amplitudes recorded in bands 11, 12, and 16 are consistently lower

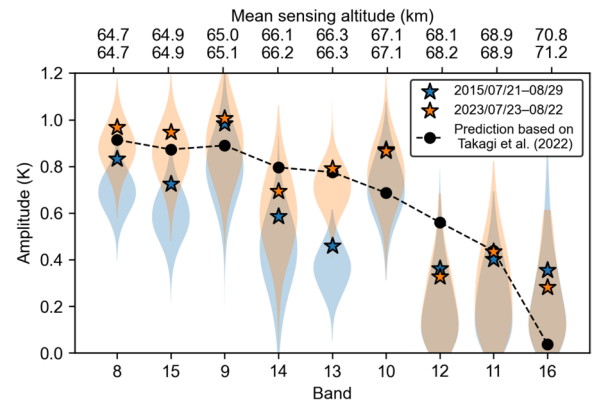


Fig. 10 Amplitude in temperature detected at the period of 5 days. The blue and orange stars show analysis results from Fig. 9b and d, respectively. The blue and orange violin plots show the probability density of the true value of the temperature amplitude. The black line shows amplitudes at each band predicted with the GCM simulation data (Takagi et al. 2022). The corresponding mean sensing altitudes of Himawari-8 and –9 are labeled in the upper x-axis

than those in the other bands, indicating that this discrepancy cannot be attributed to observational bias.

Figure 10 also suggests a temporal variation of the Rossby wave structure between the two observation periods. While the probabilities of true amplitudes at bands 11, 12, and 16 remain nearly identical for the two periods, the probabilities for lower-altitude bands are distributed around larger amplitudes during 2023/07/23–08/22 than during 2015/07/21–08/29. This difference in amplitude between the two periods is statistically significant. Comparing the distribution of the true amplitude estimated in our Bayesian analyses between two observation periods, the amplitude in 2023/07/23–08/22 is higher than that in 2015/07/21–08/29 with probabilities of 99.7%, 95.2%, and 92.8% at bands 13, 15, and 8, respectively.

5 Discussion

5.1 Implications for temporal variations in the Venus atmosphere

The observed variation in the thermal tide structure may be linked to variations in albedo and zonal wind speed. Lee et al. (2019) showed that the Venus albedo at 365 nm varied by a factor of two between 2006 and 2017. Using the Venus Planetary Climate Model (PCM), they also indicated that causal variation in solar heating rate can account for zonal wind speed variation observed by Khatuntsev et al. (2013), Kouyama et al. (2013), Hueso et al. (2015), and Horinouchi et al. (2018). Since the thermal tide is excited by solar heating, these variations might be correlated with the thermal tide structure. While definitive conclusions are challenging due to the limited temporal resolution of the AHI data, comparison with the latest wind speed analysis (Horinouchi et al. 2024) suggests a potential negative correlation between the wind speed and diurnal tide amplitude. For instance, at the local time of 6 h, the brightness temperature decreases with time in the four observation periods of AHI between 2015 and 2023 (Fig. 8), meaning an increase in the diurnal tide amplitude. On the other hand, the wind speed observations around the same timeframe as AHI show a decrease with time (Fig. 7a in Horinouchi et al. 2024).

The multiband measurement by AHI also suggests the possibility that a change in static stability structure may also be associated with the observed variations in the thermal tide patterns. A sensitivity study by Suzuki et al. (2022) shows that an increase in static stability at altitudes between 60 and 80 km can weaken the diurnal thermal tide structure. As shown in Fig. 8, the amplitude of the diurnal tide in 2015 was larger than that in 2023. Notably, this change in amplitude coincides with a shift in the vertical temperature profile. Figure 11 depicts the temperature difference around midnight between 2015 and 2023. While the temperatures below 70 km were

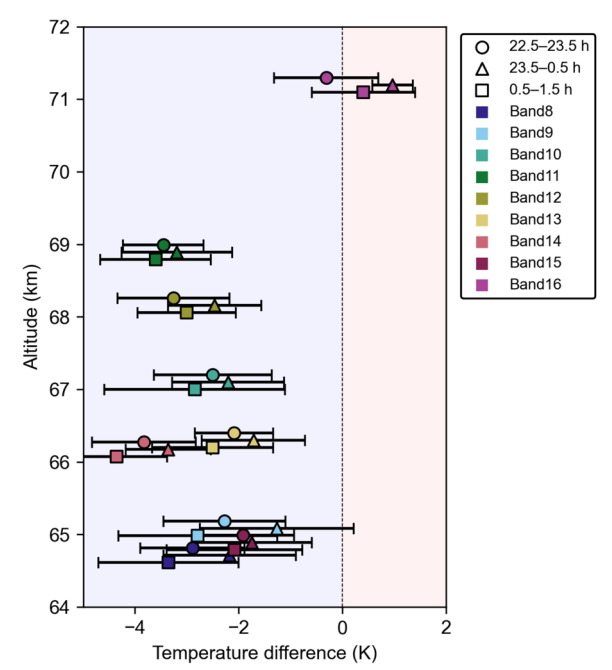


Fig. 11 Midnight temperature difference between 2015/07/21–08/29 and 2023/07/23–08/22 observed by AHI. The x-axis represents the temperature measured in the second period after subtracting that in the first one. The circles, triangles, and squares with error bars show the average and standard deviations of the brightness temperature difference at local-time bins of 22.5–23.5, 23.5–0.5, and 0.5–1.5 h, respectively. For clarity, the altitudes of the circles and squares are shifted by +0.1 and -0.1 km, respectively

lower in 2023 than in 2015, band 16 indicates higher temperatures above 70 km in 2023. This altitude-dependent variation suggests an increase in stability in 2023 compared to 2015, implying a qualitatively consistent relationship in diurnal tide amplitude between the AHI observation and numerical model predictions. Note that these observation periods were covered by different AHIs onboard Himawari-8 and -9; however, these temperature differences are larger than sensitivity difference between the two AHIs (Zhu et al. 2024) and, therefore, cannot be attributed to the instrument functionality.

The variation in the planetary-wave structure is consistent with that in thermal tides as shown by previous works. According to the LIR data analysis by Lai and Li (2023), the 5-day Rossby-wave amplitude in temperature exhibits variations with a period of approximately 220 days. They also show a correlation with the vertical shear of the zonal wind modulated by the thermal tides. While the periods during which AHI was able to extract periodicity information cannot be compared with their analysis because of time gaps, the AHI observation of thermal tides and Rossby waves is consistent with the correlation shown by Lai and Li (2023). Both the diurnal thermal tide and Rossby-wave amplitudes are smaller in

2015 than in 2023. As discussed for the thermal tides, the observed variation in planetary-scale waves may be caused by factors like the super-rotation speed and could have a periodic pattern (e.g., Kouyama et al. 2013, 2015). While periodicity cannot be inferred solely from the scarce observations at the same local time by AHI, these data can be used as complementary data to fill gaps until cloud-tracking observations become available in the future.

It is noteworthy that the observed dependency of 5-day Rossby-wave amplitude on altitude is qualitatively consistent with previous numerical simulations but might not completely match these predictions. Previous studies of 5-day Rossby waves with Venus Global Climate Model (GCM) by Takagi et al. (2022) and Lai et al. (2024) show that the amplitude of temperature deviation peaks around 65 km. Due to the steep phase tilt above 70 km, the temperature deviation begins to decrease with altitude and gets reversed. It is predicted that the temperature deviation approaches zero at altitudes between 70 and 75 km, varying with latitude. The black line in Fig. 10 shows the prediction by Takagi et al. (2022) after convoluting the distribution of local time, latitude, and emission angles to compare with the AHI observations. This overall trend of decreasing with increasing altitude qualitatively agrees with the AHI observation (Fig. 10). For example, the weighting function shows that the temperature observed at band 16 incorporates contributions from both above and below 70 km (Fig. 6), leading to a cancellation of temperature deviations in Fig. 10. At the other bands, the observed radiance mostly originates from altitudes below 70 km (Fig. 6) and is expected to have larger amplitudes than at band 16. However, the amplitudes observed at bands 11 and 12 shows amplitudes as low as band 16. These measurements do not completely match the numerical simulations, particularly in the period in 2023 (black dashed line in Fig. 10). Future GCM simulations with a variety of physical parameters might resolve this discrepancy and could provide insight into the thermal dynamics of the planetary-scale waves on Venus.

5.2 Further utility as a Venus-monitoring satellite

The findings discussed above demonstrate that AHI is capable of acquiring Venus temperatures at various time intervals. These data sets are useful not only for calibration, but also for tracking the temporal variation and altitude structure of thermal tide and planetary-scale waves. Particularly in the upcoming years, these meteorological data might be the only available spaceborne monitoring data of Venus in the infrared wavelengths. If the communication with the Akatsuki spacecraft is not established again, no additional data will be obtained by LIR. Furthermore, the future spectral measurements planned in the

NASA Discovery VERITAS and ESA EnVision missions do not cover wavelengths exceeding 2.5 μ m (Helbert et al. 2016, 2019). The Himawari-8 and 9 are supposed to end their operation in 2029 and will be replaced by a new meteorological satellite. Because the successors of Himawari-9 are expected to have similar infrared coverages, they can continue to serve as unique and precious eyes for Venus science to complement the lack of spaceborne data. Such successive measurements of Venus are also expected to be conducted by other meteorological satellites like the GOES satellites (Fulbright et al. 2023), which have almost the same wavelength coverage as the Himawari series.

The utility of these meteorological satellites may extend further in the Venus community. For example, simultaneous measurement with ground-based telescopes might provide more insights into episodic SO₂ plumes in the Venus atmosphere. Encrenaz et al. (2023) report anomalous increases in temperature and SO₂ in September and November 2021, possibly linked to mountain waves. They report that these temperature plumes started at the lower altitude and became visible at high-altitude bands with a time lag of a couple of days. Unfortunately, these observation timeframes were not covered by the AHI observation periods; however, simultaneous multiband measurement of AHI would help to understand these events if data are obtained at the same time in the future. In addition, variations in SO₂ abundance may influence the observed radiance at band 10. As shown in Fig. 2, the response function of band 10 overlaps with the SO₂ v3 band (7.35 μm). Mid-infrared spectra obtained by the Venera-15 mission occasionally exhibit a decrease in brightness temperature that is large enough to be detected by AHI (e.g., Oertel et al. 1985; Zasova et al. 2004). The SO₂ variation can change the sensing altitude of band 10 (Fig. 6) and might explain relatively large amplitudes of the 5-day wave at band 10. However, such analysis is out of scope of this paper because of difficulty to disentangle various factors like cloud thickness solely with the AHI data. Moreover, the AHI data at visible to near-infrared bands could be beneficial as well. Since the albedo of Venus varies in time by 20% (Lee et al. 2019), such albedo variations may be monitored with multiband observations continuously. While these measurements cannot provide spatially resolved images, the spectral resolution of AHI will provide useful data for understanding the atmospheric dynamics and its variation in Venus over decades.

6 Conclusion

This study highlights the potential of Japanese meteorological satellites, Himawari-8 and -9, as valuable space telescopes for Venus science. At the infrared bands, the

apparent Venus size is limited to only 5 pixels or less; however, their frequent calibration and multiband operation occasionally provide spaceborne and spectrally resolved measurements of disk-integrated radiance. These datasets can be used for calibrations of infrared radiometers onboard planetary missions, such as Akatsuki and BepiColombo. Our comparison among AHI, LIR, and MERTIS suggests that LIR might have underestimated the Venus radiance by 15–17%, which should be considered for future analysis of the LIR data.

AHI is capable of detecting temporal variation of the Venus temperature structure. The multiband measurement at the mid-infrared wavelengths allows for the sensing of temperature across different altitudes, ranging from 64 to 71 km. Although Venus cannot be resolved spatially, the dependence of the brightness temperature on local time clearly illustrates the thermal tide structure. During the observation from 2015 to 2024, AHI succeeded in capturing variations in the diurnal thermal tide amplitude, perhaps related to decadal variation in the Venus atmosphere structure. When the apparent size of Venus is at maximum, AHI can also monitor the behavior of planetary-scale waves and altitudinal dependency. The brightness temperatures observed in periods of 2015/07/21-08/29 and 2023/07/23-08/22 show the 5-day Rossby waves, whose amplitudes are revealed to decrease with altitude. Furthermore, our Bayesian analysis confirms that the amplitudes of the 5-day Rossby waves vary in time. These temporal variations may be attributed to multiple processes, one of which is a change in stability structure detected by the AHI multiband measurements.

Infrared cameras onboard meteorological satellites like AHI will continue to provide occasional access to the Venus temperature in the coming years. Even after the retirement of the current meteorological satellites, newgeneration satellites will be launched continuously due to the importance of weather observations. Particularly at mid-infrared wavelengths, future spaceborne observation by the planned Venus missions will not be conducted for a while. Because AHI covers not only infrared spectral features of CO2, SO2, and H2SO4 aerosols, but also visible to near-infrared wavelengths, the utility may extend further in Venus science. Although AHI cannot resolve Venus spatially, integration of these datasets will enhance our ability to monitor changes over time and contribute to our understanding of the complex processes occurring within the Venus atmosphere in the future.

Appendix

Method of Venus radiance retrieval

To retrieve the Venus radiance from HSD, we first estimated the position of Venus in the AHI images with the

Spacecraft, Planet, Instrument, Camera- matrix, Events (SPICE) Toolkit (Acton et al. 2018; Annex et al. 2020). Predicting the Venus position in each AHI image taken every 10 min, we collected all the HSD in which Venus could be captured. We next examined all the collected HSD to see whether Venus is successfully captured or not. Since the scanned timing of Venus and scanned area in space are not exactly the same for all the bands, this investigation was done separately for each band in the same way as Nishiyama et al. (2022). If Venus

is overlapped by the terrestrial atmosphere, scanning swaths, or edges of scanned area, the data were removed from the latter analysis to avoid possible artifacts in the archived datasets.

The aperture-photometry technique was then used to calculate the disk-integrated radiance after correcting for the background radiance based on the radiance at pixels surrounding Venus. Outside the Earth, there is non-zero radiance as a function of distance from the Earth (Fig. 12a). This background radiance is likely due to stray

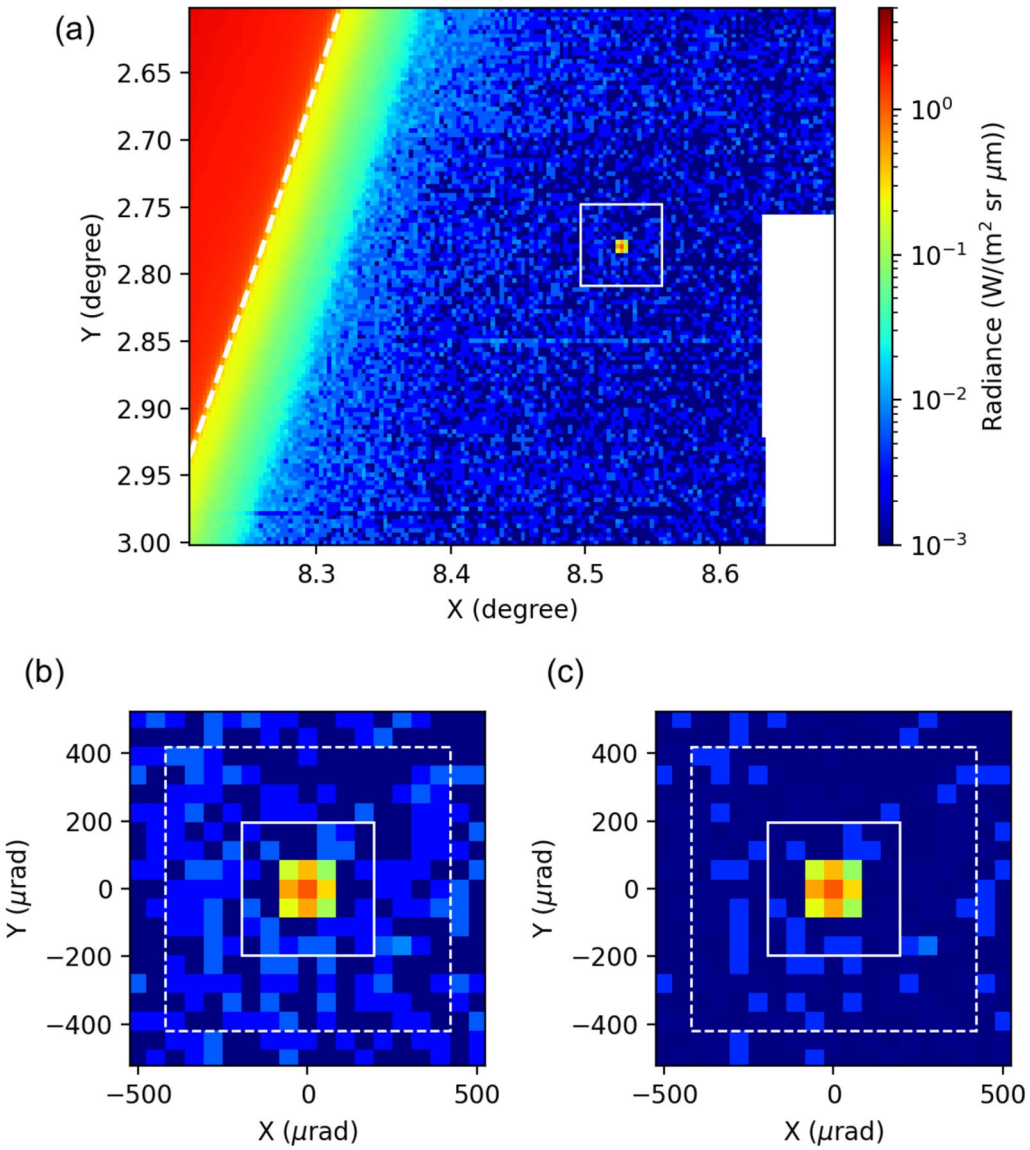


Fig. 12 Demonstration of the background correction. **a** Radiance data around Venus taken at 18:00 on 2018/08/11. The white dashed line corresponds to the rim of the Earth. The white area on the right side is outside the scanned swath. The white square highlights the area zoomed in **b** and **c**. **b** Pre-correction data around Venus. **c** Post-correction data around Venus. The white dashed and solid lines show areas used for radiance summation and background estimation.

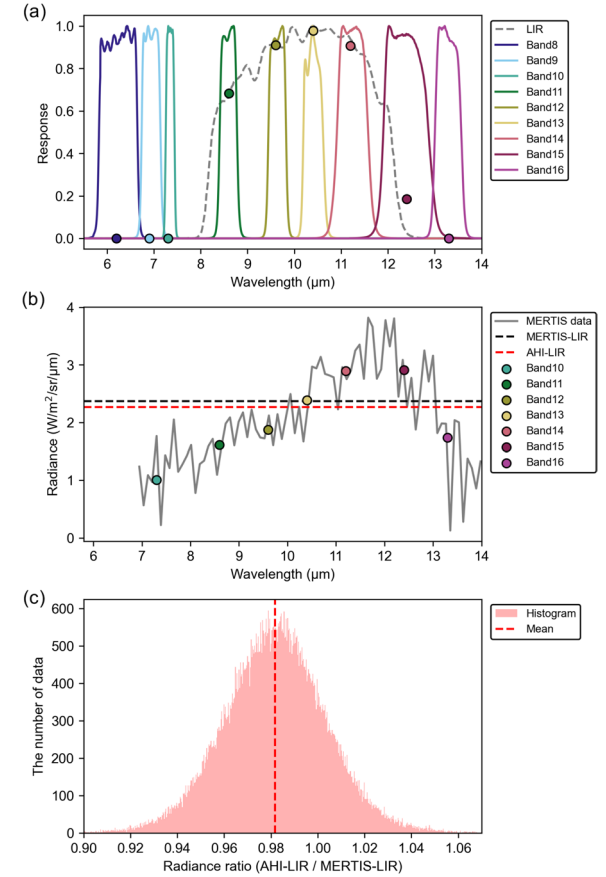


Fig. 13 Demonstration of spectral comparison among AHI, LIR, and MERTIS. a Response functions of AHIs and LIR and weighting coefficients. The solid lines show the AHI response functions for Himawari-8. The LIR response function is shown as the dashed black line. The colored points show weighting coefficients for each AHI band (i.e., c_k in Eq. (1)). **b** Example of spectral convolution. The gray line shows one of the MERTIS measurements during the flyby. The colored points show the simulated AHI data from this MERTIS measurement. Note that bands 8 and 9 are excluded because they observe radiance outside the MERTIS coverage. The black dashed line shows the simulated LIR measurement from the MERTIS measurement. The red dashed line shows the LIR measurement convolved from the simulated AHI measurements. **c** Histogram of ratios of the AHI data after the LIR response convolution to the simulated LIR. The red dashed line shows the mean of the ratios.

light (Nishiyama et al. 2022; Taniguchi et al. 2022) and needs to be corrected to estimate the radiance of celestial bodies. Following Taniguchi et al. (2022), the background level is estimated by fitting a two-dimensional polynomial to the radiance values which are located outside the aperture square and inside twice the aperture square (namely, area between white solid and dashed squares in Fig. 12b and c). The polynomial order was chosen from 0 to 4 by minimizing the Akaike information criterion. After subtracting the estimated

background within the aperture square (Fig. 12c), we summed the radiance within the aperture to derive the disk-integrated radiance. Since the apparent Venus diameter varies from 0.84 to 5.1 pixels, depending on its distance from the Earth, the aperture size was determined by summing twice the apparent diameter with a point-spread-function scale of 2 pixels. If this value is less than 7 pixels, the aperture size is fixed to 7 pixels, following Taniguchi et al. (2022).

Method of spectral comparison among AHI, LIR, and MERTIS

To compare radiance data from the three instruments with different response functions, radiance data with higher spectral resolution needs to be convolved with the response function of the other instrument. In the case of the MERTIS-LIR comparison, the MERTIS hyperspectral data are convolved with the LIR response function. However, the AHI-LIR comparison is not as straightforward as the MERTIS-LIR comparison because the wavelength coverages of the AHI bands are wide and distributed sparsely. To sum up the AHI data to compare to the LIR data, we first derived weighting coefficients for each AHI band, $\overline{c_k}$:

$$c_k = \int f_{\text{LIR}} f_{\text{AHI}-k} d\lambda, \tag{1}$$

$$\overline{c_k} = \frac{c_k}{\sum_k c_k},\tag{2}$$

where $f_{\rm LIR}$ is the response function of LIR, $f_{\rm AHI}$ is the response function of AHI at band k, λ is wavelength. Then, the AHI data convolved with the LIR response function, $R_{\rm AHI}$ is calculated as:

$$R_{\text{AHI-LIR}} = \sum_{k} \overline{c_k} R_{\text{AHI}-k}, \tag{3}$$

where $R_{\mathrm{AHI}-k}$ is the radiance measured by AHI at band k. Therefore, the Venus radiance outside the LIR spectral coverage is filtered out in the comparison process, and the variation in response within the LIR coverage is also taken into account as shown in Fig.

13a

The comparison method is validated using the Venus hyperspectral data from MERTIS. The approach in this study might contain a systematic bias because the AHI bands do not fully cover the wavelengths of the LIR response function. For example, the emission peak of Venus lies in the gap between the coverages of band 14 and 15. Such features are covered by the LIR response function but missed by the AHI response functions, potentially leading to an underestimation in

the comparison based on our convolution method. To quantify the bias, we used hyperspectral data acquired by MERTIS during the BepiColombo flyby as a reference (Helbert et al. 2023). Although each MERTIS data is noisy due to the low cloud-top temperature of Venus (gray line in Fig. 13b), a number of the obtained spectral profiles allows us to test our method over a wide range of longitude, latitude, and emission angles. We first simulate the LIR and AHI observations by convolving the MER-TIS spectrum with the response functions (the black dashed line and colored points in Fig. 13b). Then, the simulated AHI measurements are summed up based on Eqs. (1), (2) and (3) (the red dashed line in Fig. 13b) and compared with the simulated LIR one. Figure 13c shows all the application results as a histogram of the ratios of the AHI-convolved LIR to the simulated LIR. While the result is widely scattered due to the noise in the MERTIS data, this simulation ensures that our method of comparing AHI and LIR introduces only a minor artifact, with an average of 2% or less.

Abbreviations

AHI Advanced Himawari Imager
GCM Global Climate Model
HSD Himawari Standard Data
JMA Japan Meteorological Agency
LIR Longwave infrared camera

MERTIS Mercury Radiometer and Thermal Infrared Spectrometer

RMS Root-mean-square PCM Planetary Climate Model

Acknowledgements

This work was supported by JSPS KAKENHI Grant Number JP22 K21344, 23H00150, and 23H01249, and JSPS Overseas Research Fellowship. The authors are grateful to two anonymous reviewers for their careful and constructive review comments. Open Access funding enabled and organized by Projekt DEAL.

Author contributions

GN investigated all the data, wrote the original draft, and finalized the manuscript. GN and SU established the methodology. GN, US, and SU conceptualized the research. SA, TI, TI, YF, TM, MT, TK, OB, MD, JH, SA and HH contributed to the scientific discussion. All the authors read and approved the final manuscript.

Funding

Open Access funding enabled and organized by Projekt DEAL. This work was supported by JSPS KAKENHI Grant Number JP22 K21344, 23H00150, and 23H01249, and JSPS Overseas Research Fellowship. Open Access funding enabled and organized by Projekt DEAL.

Availability of data and materials

All HSD are collected and provided under the Data Integration and Analysis System (DIAS), which was developed and operated by a project supported by the Ministry of Education, Culture, Sports, Science, and Technology. The L3d LIR product is publicly available at the JAXA archive website, DARTS. The MERTIS data obtained during the Venus flyby are open to public: https://doi.org/10.6084/m9.figshare.24476812.v1. The archived Venus data may be shared upon reasonable request to GN.

Declarations

Ethics approval and consent to participate

Not applicable.

Consent for publication

Not applicable.

Competing interests

The authors declare that they have no competing interests.

Author details

Institute of Space Research, German Aerospace Center (DLR), Rutherfordstraße 2, 12489 Berlin, Germany. ²Department of Earth and Planetary Science, Graduate School of Science, The University of Tokyo, Tokyo 113-0033, Japan. ³National Astronomical Observatory of Japan, Tokyo 181-8588, Japan. ⁴Institute of Space and Astronautical Science (ISAS), Japan Aerospace Exploration Agency (JAXA), Kanagawa 252-5210, Japan. ⁵Institute of Astronomy, Graduate School of Science, The University of Tokyo, Mitaka 181-0015, Japan. ⁶Graduate School of Frontier Sciences, The University of Tokyo, Chiba 277-0882, Japan. ⁷Max-Planck-Institut Für Extraterrestrische Physik, 85748 Garching, Germany. ⁸College of Science, Rikkyo University, Tokyo 171-8501, Japan. ⁹Digital Architecture Research Center, National Institute of Advanced Industrial Science and Technology, Tokyo 135-0064, Japan. ¹⁰European Space Research and Technology Centre (ESTEC), European Space Agency (ESA), Keplerlaan 1, 2200 Noordwijk, The Netherlands. 11 Institut Für Planetologie, Universität Münster, Wilhelm-Klemm-Straße 10, 48149 Münster, Germany. 12 Present Address: Center for Advanced Photonics, RIKEN, Wako 351-0198, Japan.

Received: 22 January 2025 Accepted: 19 May 2025 Published: 30 June 2025

References

- Acton C, Bachman N, Semenov B, Wright E (2018) A look towards the future in the handling of space science mission geometry. Planet Space Sci 150:9–12. https://doi.org/10.1016/j.pss.2017.02.013
- Akiba M, Taguchi M, Fukuhara T et al (2021) Thermal tides in the upper cloud layer of venus as deduced from the emission angle dependence of the brightness temperature by Akatsuki/LIR. J Geophys Res Planets 126:1–12. https://doi.org/10.1029/2020JE006808
- Annex A, Pearson B, Seignovert B et al (2020) SpiceyPy: a Pythonic Wrapper for the SPICE Toolkit. J Open Source Softw 5:2050. https://doi.org/10.21105/ioss.02050
- Bauch KE, Hiesinger H, Greenhagen BT, Helbert J (2021) Estimation of surface temperatures on Mercury in preparation of the MERTIS experiment onboard BepiColombo. lcarus. https://doi.org/10.1016/j.icarus.2020. 114083
- Burgdorf MJ, Taniguchi D (2024) Checking the radiometric stability of infrared imagers with Venus. In: IGARSS 2024—2024 IEEE international geoscience and remote sensing symposium. IEEE. pp 6201–6204
- D'Amore M, Helbert J, Maturilli A, et al (2018) Data processing of the Mercury radiometer and thermal infrared imaging spectrometer (MERTIS) onboard Bepi Colombo. 16. https://doi.org/10.1117/12.2321051
- Del Genio AD, Rossow WB (1990) Planetary-scale waves and the cyclic nature of cloud top dynamics on Venus. J Atmos Sci 47:293–318. https://doi.org/10.1175/1520-0469(1990)047%3c0293:PSWATC%3e2.0.CO;2
- Encrenaz T, Greathouse TK, Roe H et al (2012) HDO and SO 2 thermal mapping on Venus: evidence for strong SO 2 variability. Astron Astrophys 543:1–7. https://doi.org/10.1051/0004-6361/201219419
- Encrenaz T, Greathouse TK, Richter MJ et al (2016) HDO and SO 2 thermal mapping on Venus. Astron Astrophys 595:A74. https://doi.org/10.1051/0004-6361/201628999
- Encrenaz T, Greathouse TK, Marcq E et al (2020) HDO and SO2thermal mapping on Venus: V. Evidence for a long-term anti-correlation. Astrophys 639:1–11. https://doi.org/10.1051/0004-6361/202037741
- Encrenaz T, Greathouse TK, Giles R et al (2023) HDO and SO $_2$ thermal mapping on Venus. Astron Astrophys 674:A199

- Fels SB, Lindzen RS (1974) The interaction of thermally excited gravity waves with mean flows. Geophys Fluid Dyn 6:149–191. https://doi.org/10.1080/03091927409365793
- Fukuhara T, Taguchi M, Imamura T et al (2011) LIR: Longwave infrared camera onboard the venus orbiter Akatsuki. Earth Planets Space 63:1009–1018. https://doi.org/10.5047/eps.2011.06.019
- Fukuhara T, Taguchi M, Imamura T et al (2017) Absolute calibration of brightness temperature of the Venus disk observed by the Longwave Infrared Camera onboard Akatsuki Akatsuki at Venus: The First Year of Scientific Operation Masato Nakamura, Dmitri Titov, Kevin McGouldrick, Pierre Drossart, Jean-Lo. Earth Planets Space 69:1–9. https://doi.org/10.1186/s40623-017-0727-y
- Fulbright JP, Pogorzala D, Kline E (2023) Calibration of GOES-R ABI Data Using Celestial Targets. International geoscience and remote sensing symposium (IGARSS) 2023-July. pp 4502–4505. https://doi.org/10.1109/IGARS S52108.2023.10282380
- Gordon IE, Rothman LS, Hargreaves RJ et al (2022) The HITRAN2020 molecular spectroscopic database. J Quant Spectrosc Radiat Transf 277:107949. https://doi.org/10.1016/j.jgsrt.2021.107949
- Griffith PC (2015) Advanced Himawari Imager (AHI) design and operational flexibility. Tokyo, Japan
- Haus R, Kappel D, Arnold G (2013) Self-consistent retrieval of temperature profiles and cloud structure in the northern hemisphere of Venus using VIRTIS/VEX and PMV/VENERA-15 radiation measurements. Planet Space Sci 89:77–101. https://doi.org/10.1016/j.pss.2013.09.020
- Helbert J, Wendler D, Walter I, et al. (2016) The Venus Emissivity Mapper (VEM) concept. Infrared remote sensing and instrumentation XXIV 9973:99730R. https://doi.org/10.1117/12.2237568
- Helbert J, Vandaele AC, Marcq E, et al (2019) The VenSpec suite on the ESA EnVision mission to Venus. 1112804:6. https://doi.org/10.1117/12.25292
- Helbert J, Haus R, Arnold G et al (2023) The second Venus flyby of BepiColombo mission reveals stable atmosphere over decades. Nat Commun. https://doi.org/10.1038/s41467-023-43888-7
- Hiesinger H, Helbert J (2010) The Mercury Radiometer and Thermal Infrared Spectrometer (MERTIS) for the BepiColombo mission. Planet Space Sci 58:144–165. https://doi.org/10.1016/j.pss.2008.09.019
- Hiesinger H, Helbert J, Alemanno G et al (2020) Studying the composition and Mineralogy of the Hermean surface with the Mercury Radiometer and Thermal Infrared Spectrometer (MERTIS) for the BepiColombo mission: an update. Space Sci Rev 216:1–37
- Horinouchi T, Kouyama T, Lee YJ et al (2018) Mean winds at the cloud top of Venus obtained from two-wavelength UV imaging by Akatsuki. Earth Planets Space. https://doi.org/10.1186/s40623-017-0775-3
- Horinouchi T, Kouyama T, Imai M et al (2024) Long-term variability of mean winds and planetary-scale waves around venusian cloud top observed with Akatsuki/UVI. J Geophys Res Planets. https://doi.org/10.1029/2023J E008221
- Hou AY, Fels SB, Goody RM (1990) Zonal superrotation above Venus' cloud base induced by the semidiurnal tide and the mean meridional circulation. J Atmos Sci 47:1894–1901. https://doi.org/10.1175/1520-0469(1990)047% 3c1894:ZSAVCB%3e2.0.CO;2
- Hueso R, Peralta J, Garate-Lopez I et al (2015) Six years of Venus winds at the upper cloud level from UV, visible and near infrared observations from VIRTIS on Venus Express. Planet Space Sci 113–114:78–99. https://doi.org/10.1016/j.pss.2014.12.010
- Imai M, Kouyama T, Takahashi Y et al (2019) Planetary-scale variations in winds and UV brightness at the venusian cloud top: periodicity and temporal evolution. J Geophys Res Planets 124:2635–2659. https://doi.org/10.1029/2019JE006065
- Imamura T (2006) Meridional propagation of planetary-scale waves in vertical shear: Implication for the Venus atmosphere. J Atmos Sci 63:1623–1636. https://doi.org/10.1175/JAS3684.1
- Imamura T, Horinouchi T, Dunkerton TJ (2004) The lateral transport of zonal momentum due to Kelvin waves in a meridional circulation. J Atmos Sci 61:1966–1975. https://doi.org/10.1175/1520-0469(2004)061%3c1966: TLTOZM%3e2.0.CO;2
- Japan Meteorological Agency (2017) Himawari standard data user's guide (Version 1.3). Japan Meteorological Agency

- Kajiwara N, Imamura T, Taguchi M, Kouyama T (2021) Planetary-scale waves seen in thermal infrared images of venusian cloud top. J Geophys Res Planets 126:1–13. https://doi.org/10.1029/2021JE007047
- Kalluri S, Alcala C, Carr J et al (2018) From photons to pixels: processing data from the advanced baseline imager. Remote Sens (Basel). https://doi.org/10.3390/rs10020177
- Khatuntsev IV, Patsaeva MV, Titov DV et al (2013) Cloud level winds from the Venus express monitoring camera imaging. Icarus 226:140–158. https://doi.org/10.1016/j.icarus.2013.05.018
- Kouyama T, Imamura T, Nakamura M et al (2013) Long-term variation in the cloud-tracked zonal velocities at the cloud top of Venus deduced from Venus Express VMC images. J Geophys Res Planets 118:37–46. https://doi.org/10.1029/2011JE004013
- Kouyama T, Imamura T, Nakamura M et al (2015) Vertical propagation of planetary-scale waves in variable background winds in the upper cloud region of Venus. Icarus 248:560–568. https://doi.org/10.1016/j.icarus.2014.07.011
- Kouyama T, Taguchi M, Fukuhara T et al (2019) Global structure of thermal tides in the upper cloud layer of venus revealed by LIR on board Akatsuki. Geophys Res Lett 46:9457–9465. https://doi.org/10.1029/2019GL083820
- Lacy JH, Richter MJ, Greathouse TK et al (2002) TEXES: a sensitive high-resolution grating spectrograph for the mid-infrared. Publ Astron Soc Pac 114:153–168. https://doi.org/10.1086/338730
- Lai D, Li T (2023) Long-term variation of the quasi-five-day wave in the top layer of Venus clouds. J Geophys Res Planets. https://doi.org/10.1029/2022 IF007596
- Lai D, Lebonnois S, Li T (2024) Planetary-scale wave activity in venus cloud layer simulated by the Venus PCM. J Geophys Res Planets. https://doi.org/10.1029/2023JE008253
- Lee YJ, Jessup K-L, Perez-Hoyos S et al (2019) Long-term variations of Venus's 365 nm albedo observed by Venus express, Akatsuki, MESSENGER, and the Hubble Space Telescope. Astron J 158:126. https://doi.org/10.3847/1538-3881/ab3120
- Müller TG, Burgdorf M, Alí-Lagoa V et al (2021) The Moon at thermal infrared wavelengths: a benchmark for asteroid thermal models. Astron Astrophys. https://doi.org/10.1051/0004-6361/202039946
- Nakamura M, Imamura T, Ishii N et al (2016) AKATSUKI returns to Venus. Earth Planets Space. https://doi.org/10.1186/s40623-016-0457-6
- Nara Y, Imamura T, Murakami S et al (2019) Formation of the Y feature at the venusian cloud top by planetary-scale waves and the mean circulation: analysis of Venus express VMC images. J Geophys Res Planets 124:1143–1156. https://doi.org/10.1029/2018JE005779
- Newman M, Leovy C (1992) Maintenance of strong rotational winds in Venus' middle atmosphere by thermal tides. Science 257:647–650. https://doi.org/10.1126/science.257.5070.647
- Nishiyama G, Namiki N, Sugita S, Uno S (2022) Utilization of a meteorological satellite as a space telescope: the lunar mid-infrared spectrum as seen by Himawari-8. Earth Planets Space. https://doi.org/10.1186/ s40623-022-01662-x
- Oertel D, Spänkuch D, Jahn H et al (1985) Infrared spectrometry of Venus from "Venera-15" and "Venera-16." Adv Space Res 5:25–36. https://doi.org/10. 1016/0273-1177(85)90267-4
- Okuyama A, Takahashi M, Date K et al (2018) Validation of himawari-8/ahi radiometric calibration based on two years of in-orbit data. J Meteorol Soc Jpn 96B:91. https://doi.org/10.2151/jmsj.2018-033
- Palmer KF, Williams D (1975) Optical constants of sulfuric acid; application to the clouds of Venus? Appl Opt 14:208. https://doi.org/10.1364/ao.14. 000208
- Plumb RA (1975) Momentum transport by the thermal tide in the stratosphere of Venus. Q J R Meteorol Soc 101:763–776. https://doi.org/10.1002/qj. 49710143005
- Pollack JB, Dalton JB, Grinspoon D et al (1993) Near-infrared light from Venus' nightside: a spectroscopic analysis. Icarus 103:1–42. https://doi.org/10. 1006/icar.1993.1055
- Rossow WB, Del Genio AD, Eichler T (1990) Cloud-tracked winds from pioneer Venus OCPP images. J Atmos Sci 47:2053–2084. https://doi.org/10.1175/1520-0469(1990)047%3c2053:CTWFVO%3e2.0.CO;2
- Scargle JD (1982) Statistical aspects of spectral analysis of unevenly spaced data. Astrophys J 263:835–853

- Seiff A, Schofield JT, Kliore AJ et al (1985) Models of the structure of the atmosphere of Venus from the surface to 100 kilometers altitude. Adv Space Res 5:3–58. https://doi.org/10.1016/0273-1177(85)90197-8
- Suzuki A, Takagi M, Ando H et al (2022) A sensitivity study of the thermal tides in the venusian atmosphere: structures and dynamical effects on the superrotation. J Geophys Res Planets 127:1–23. https://doi.org/10.1029/2022JE007243
- Taguchi M, Kouyama T, Sugawa T et al (2023) In-orbit recalibration of longwave infrared camera onboard Akatsuki. Earth Planets Space 75:1–8. https://doi.org/10.1186/s40623-023-01803-w
- Takagi M, Matsuda Y (2005) Sensitivity of thermal tides in the Venus atmosphere to basic zonal flow and Newtonian cooling. Geophys Res Lett 32:1–5. https://doi.org/10.1029/2004GL022060
- Takagi M, Matsuda Y (2007) Effects of thermal tides on the Venus atmospheric superrotation. J Geophys Res Atmos 112:1–8. https://doi.org/10.1029/2006JD007901
- Takagi M, Ando H, Sugimoto N, Matsuda Y (2022) A GCM study on the 4-day and 5-day waves in the Venus atmosphere. J Geophys Res Planets. https://doi.org/10.1029/2021JE007164
- Takahashi M, Okuyama A (2017) Introduction to the Global Space-based Inter-Calibration System (GSICS) and calibration/validation of the Himawari-8/ AHI visible and infrared bands. Meteorol Satell Cent Tech Note 62:1–18 (in Japanese)
- Taniguchi D, Yamazaki K, Uno S (2022) The Great Dimming of Betelgeuse seen by the Himawari-8 meteorological satellite. Nat Astron 6:930–935. https://doi.org/10.1038/s41550-022-01680-5
- Taylor FW, Beer R, Chahine MT et al (1980) Structure and meteorology of the middle atmosphere of Venus: infrared remote sensing from the Pioneer Orbiter. J Geophys Res Space Phys 85:7963–8006. https://doi.org/10.1029/JA085iA13p07963
- Villanueva GL, Smith MD, Protopapa S et al (2018) Planetary Spectrum Generator: an accurate online radiative transfer suite for atmospheres, comets, small bodies and exoplanets. J Quant Spectrosc Radiat Transf 217:86–104. https://doi.org/10.1016/j.jgsrt.2018.05.023
- Yamamoto M, Tanaka H (1997) Formation and maintenance of the 4-day circulation in the Venus middle atmosphere. J Atmos Sci 54:1472–1489. https://doi.org/10.1175/1520-0469(1997)054%3c1472:FAMOTD%3e2.0. CO:2
- Zasova LV, Moroz VI, Formisano V et al (2004) Infrared spectrometry of Venus: IR Fourier spectrometer on Venera 15 as a precursor of PFS for Venus express. Adv Space Res 34:1655–1667. https://doi.org/10.1016/j.asr.2003.
- Zasova LV, Moroz VI, Linkin VM et al (2006) Structure of the Venusian atmosphere from surface up to 100 km. Cosm Res 44:364–383. https://doi.org/10.1134/S0010952506040095
- Zhu Z, Gu J, Xu B, Shi C (2024) Characterization of Himawari-8/AHI to Himawari-9/AHI infrared observations continuity. Int J Remote Sens 45:121–142. https://doi.org/10.1080/01431161.2023.2293476

Publisher's Note

Springer Nature remains neutral with regard to jurisdictional claims in published maps and institutional affiliations.